Aeolian Impact Ripples in Sand Beds of Varied Texture

A Thesis Submitted to the Committee on Graduate Studies in Partial Fulfillment of the Requirements for the Degree of Master of Science in the Faculty of Arts and Science

TRENT UNIVERSITY

Peterborough, Ontario, Canada

Environmental and Life Sciences M.Sc. Graduate Program

May 2013

Abstract

AEOLIAN IMPACT RIPPLES IN SAND BEDS OF VARIED TEXTURE

K. ottO Bédard

A wind tunnel study was conducted to investigate aeolian impact ripples in sand beds of varied texture from coarsely skewed to bimodal. Experimental data is lacking for aeolian megaripples, particularly in considering the influence of wind speed on ripple morphometrics. Additionally, the modelling community requires experimental data for model validation and calibration.

Eighteen combinations of wind speed and proportion of coarse mode particles by mass were analysed for both morphometrics and optical indices of spatial segregation. Wind tunnel conditions emulated those found at aeolian megaripple field sites, specifically a unimodal wind regime and particle transport mode segregation. Remote sensing style image classification was applied to investigate the spatial segregation of the two differently coloured size populations.

Ripple morphometrics show strong dependency on wind speed. Conversely, morphometric indices are inversely correlated to the proportion of the distribution that was comprised of coarse mode particles. Spatial segregation is highly correlated to wind speed in a positive manner and negatively correlated to the proportion of the distribution that was comprised of coarse mode particles. Results reveal that the degree of spatial segregation within an impact ripple bedform can be higher than previously reported in the literature.

Acknowledgements

I would like to acknowledge all the people who have contributed in some way or other to this research project. Dr. Cheryl McKenna Neuman deserves a great deal of credit for taking me on as a graduate student and providing extensive guidance throughout this process. Her belief in my abilities provided the motivation and confidence needed to take on this endeavour.

The Trent Environmental Wind Tunnel would not have been as wonderful and fun to work in without the assistance of Patrick O'Brien, MSc. and Dr. Bailiang Li – who provided both technical expertise and a considerable amount of humour.

My partner Jennifer is most deserving of accolades for not only supporting me throughout this project, but also for listening to me and discussing it with me over the last two years. Her support, motivation, and encouragement made this project possible. For delivered dinners to the wind tunnel, and for all the missed summer adventures – thank you.

Lastly, I would like to acknowledge the financial support of BMO through the QEII-GSST scholarship.

TABLE OF CONTENTS

List of Figures

List of Tables

List of Equations

List of Symbols and Abbreviations

u_*- Shear or friction velocity

u_{*t} – Threshold friction velocity

U_∞ - Freestream velocity

d_{50} – mean particle diameter

$\%_C$ – Proportion of coarse mode particles in particle size distribution, by mass

β_C – Proportion of coarse mode particles on the surface of the sand bed, by area

β_E – Proportion of image considered an edge, by pixel

CAM – Cellular Automaton Model

DEM – Digital Elevation Model

DP – Drift Potential

DSLR – Digital Single Lens Reflex

LDA – Laser Doppler Anemometer

MP – Megapixel

PSA – Particle size analysis

PSAR – Perimeter to surface area ratio

PSD – Particle size distribution

TAR – Transverse Aeolian Ridge

Vivid – Konica-Minolta Vivid 9i non contact digitizer

Chapter 1 Introduction

1.1 Overview

Impact ripples are the most widespread of all aeolian bed forms (Lancaster, 1995). A flat sand surface, when subject to wind, will quickly self-organize into a regular pattern of ripples. Aeolian impact ripples are often a good indicator of recent, localized wind regimes as their form is quick to evolve and generally contains crests aligned perpendicular to the wind flow (Lancaster, 1995). If given sufficient time with specific sediment transport characteristics, aeolian impact ripples may grow to be very large in both amplitude and wavelength. Megaripples are the largest form of impact ripples and have been observed with wavelengths as long as 44 m (Milana, 2009). Megaripples are found globally, with notable field research reported from the Arctic, Israel, Argentina, and Antarctica (Lancaster, et al., 2002; Karnieli, et al., 2008; Yizhaq, 2008; Milana, 2009).

The conditions that result in the development of aeolian impact ripples were discussed in detail in the work of Bagnold (1941) which have been revised through the work of Sharp (1963) and Anderson (1987, 1990). Megaripples lie on the continuum of impact ripples (Lancaster, 1995), with specific environmental and particle size distribution requirements known from field studies (Yizhaq, et al., 2004; Yizhaq, 2008; Yizhaq, 2005; Milana, 2009; Milana, et al., 2010; Isenburg, et al., 2011). Numerical modelling exercises have furthered the investigation into the evolution of megaripples, specifically with the ability to compress time (Yizhaq, et al., 2004; Yizhaq, 2005; Yizhaq, 2008; Manukyan & Prigozhin, 2009). The recent advancement of cellular automaton models (CAM) has also increased our ability to simulate megaripple bed forms found on Earth and Mars (Neild & Baas, 2008; Eastwood, et al., 2011).

The development of aeolian megaripples requires three conditions - a unimodal wind regime, a bimodal particle size distribution, and sufficient time (Yizhaq, et al., 2004; Isenburg, et al., 2011). While the ranges for these basic constraints are known for the existence of megaripples, it is still unclear what influence wind speed and particle size distribution have on the morphometrics of the bedform (Isenburg, et al., 2011). Further, there are few quantitative data available from wind tunnel experiments to calibrate model results, particularly when considering the surface sorting of particles (Yizhaq, 2008; Manukyan & Prigozhin, 2009; Isenburg, et al., 2011). This thesis aims to address a number of deficiencies in the experimental knowledge base for aeolian impact ripples, particularly those comprised of bimodal particle size distributions.

In order to further explain the core objectives of this research (§1.5), and the methodology employed to achieve the objectives (Chapter 2), a brief review of the aeolian transport system, aeolian megaripple evolution, and numerical model approaches is provided in the following sections.

1.2 The Aeolian Sediment Transport System

The interaction between wind and a sand surface is a complex system with many feedback loops. A number of reference works are available on the subject (Bagnold, 1941; Greeley & Iverson, 1985; Lancaster, 1995; Pye & Tsoar, 1990; Shaio, 2008), and therefore a summary of only the pertinent information is provided in the following discussion.

Considering a representative particle within a sand bed that is exposed to air flow, the relevant forces acting upon the particle are shown in Figure 1-1. The fluid drag force, F_d, is

proportional to the square of the wind speed. Lift forces, F_l, act to lift the particle vertically out of the bed. Gravity, F_g, acts in a downward direction, and is proportional to the particle diameter, d, and density, ρ. Interparticle forces, I_p, act to bind particles together within the bed and are derived from static cohesion and pore water pressure. Particle shape and packing density can greatly influence the frictional forces between particles (Greeley & Iverson, 1985; Lancaster, 1995). In many cases, the complexity of modelling these forces results in the use of idealized, spherical particles of uniform density and diameter (Bagnold 1941; Greeley and Iversen 1985; Lancaster 1995; Shao 2008). Sand beds in the field commonly consist of particles from the same mineral source with a strongly unimodal particle size distribution, although it is not uncommon to find bi-modal and tri-modal distributions.

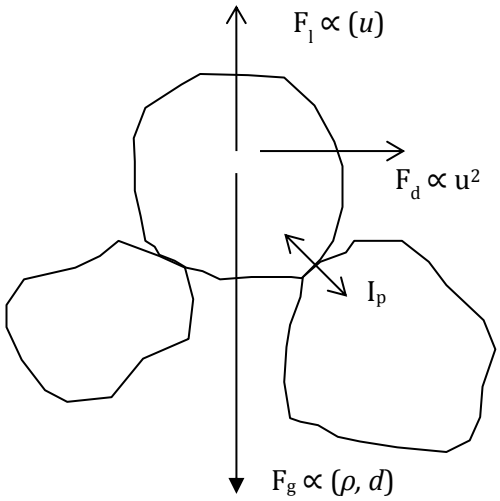

Figure 1-1 Relevant forces for a typical particle in a sand bed, after Bagnold (1941) and Greeley & Iverson (1985)

When a wind force acts on the sand bed with a velocity, u, a portion of the momentum is imparted to the particles on the sand bed. The result is the development of a shearing

(frictional) force between the air flow and the bed. The loss of momentum within the air flow is seen in typical log-linear velocity profiles for air flow, as shown in Figure 1-2. The friction velocity, u_*, is a measure of the shear stress acting on the bed surface. The friction velocity can be calculated from velocity profile data using the Prandtl-von Karman equation:

$$u_{(z)} = \frac{u_*}{k} ln\left(\frac{z}{z_0}\right) \qquad \text{Equation 1-1}$$

The wind speed at height z is denoted by $u_{(z)}$, the aerodynamic roughness length is z_0, and k is von Karman's constant (0.41). Velocity profiles are easily obtained with either pitot tube or laser Doppler anemometer instruments in a wind tunnel setting, or more crudely with anemometers mounted on meteorological towers in a field setting.

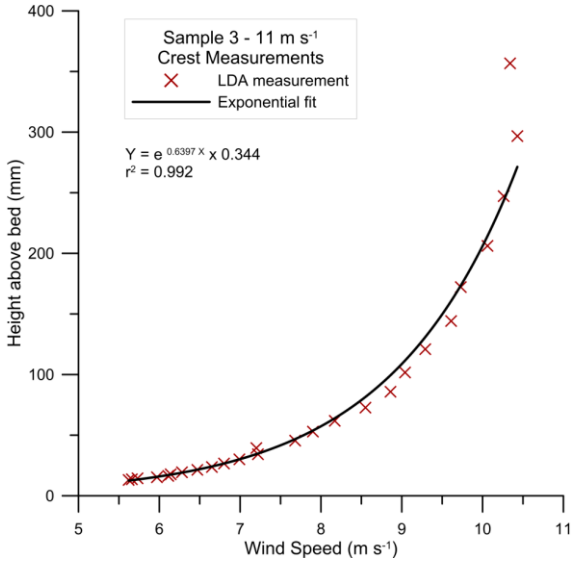

Figure 1-2 Sample of velocity profile obtained with laser Doppler anemometer showing momentum loss and zone of large shear near the bed surface.

The threshold shear velocity, u_{*t}, is reached when the shear forces are equal in magnitude and opposing in direction to the resisting forces for particle motion. Air flows are turbulent and near u_{*t} sweep and burst motions directed toward and away from the

surface, respectively, can create aerodynamic drag forces that result in particle entrainment by the flow. The shear stress required for entrainment by aerodynamic forces alone is referred to as the *fluid threshold* (Bagnold, 1941).

Entrainment results in a particle rising steeply under aerodynamic lift forces, with streamwise acceleration arising with energy transfer from the fluid flow. If the particle is sufficiently small that the turbulent motion of the air counteracts or balances the settling velocity, the particle will become *suspended* (Bagnold, 1941), see **1** in Figure 1-3. This mode of transport generally occurs only for the smallest diameter particles, typically in the dust size range. Particles in the sand size range may follow a ballistic trajectory as shown in **2**, Figure 1-3. This motion is referred to as *saltation*, as originally defined by Bagnold (1941). The height of rise and path length scale proportionally with wind speed and turbulence intensity, and scale inversely with particle diameter (Bagnold, 1941; Greeley & Iverson, 1985; Lancaster, 1995). The impact angle, α, scales inversely with wind speed and is typically between 8° - 15° (Bagnold, 1941; Lancaster, 1995). The more homogeneous the particle size distribution of the sand bed, the less variable the saltation paths followed by particles.

When a saltating particle returns to the surface it may ricochet off another bed particle, trace an additional path, and continue to move downwind. Alternatively, the collision may eject other particles that rise into the air flow and either saltate, or make a smaller hop known as *reptation*, **3** in Figure 1-3 (Anderson, 1987; Sharp, 1963).

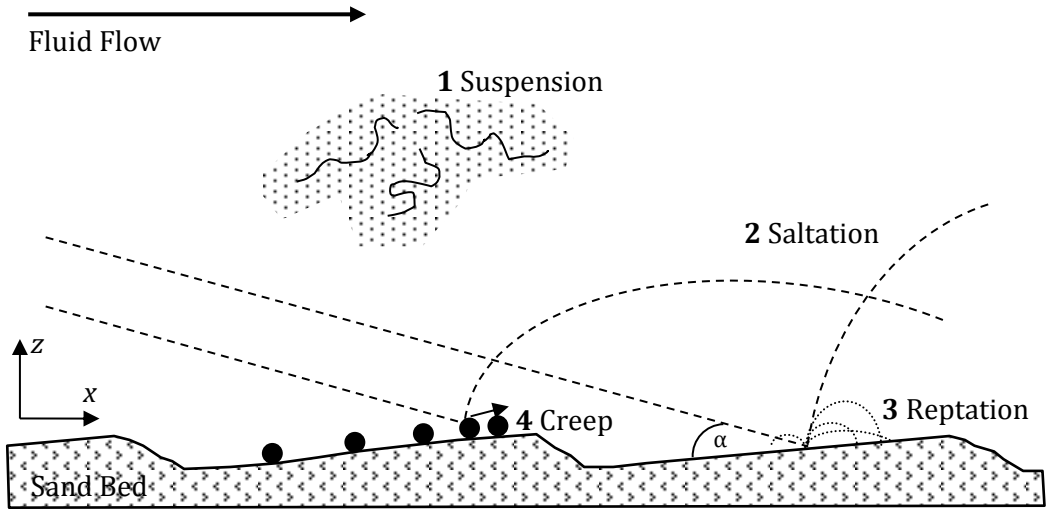

Figure 1-3 Schematic illustration of four particle transport modes (after Durán et al. 2011)

Impact with a loosely packed bed may result in a number of reptators ejected from one saltating particle as is clearly evident in Figure 1-4 (Gordon & McKenna Neuman, 2011). Reptators are distinct from saltators in that upon impacting the bed, they lack the kinetic energy either to eject other particles or to ricochet (Anderson, 1987).

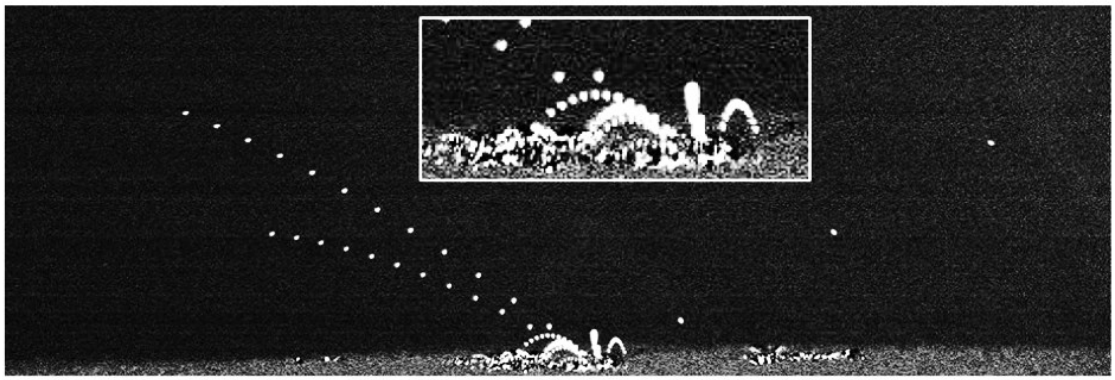

Figure 1-4 Particle tracking velocimetry image of particle ejection from a loose sand bed illustrating ejection of a number of reptators from a single saltator. Wind from right to left (after Gordon & McKenna Neuman, 2011).

The fourth mode of particle transport is *creep*, in which particles move along the surface by rolling or sliding. Fluid forces alone may cause creep, although more commonly it is driven by saltating particles that impact bed particles much larger than themselves (Bagnold, 1941; Lancaster, 1995). An impacting particle, with a low α, has sufficient energy to advance a particle with a diameter up to six times its own (Bagnold, 1941; Sharp, 1963). While saltating grains have paths that more uniformly follow the fluid direction, bedload particles may deviate from the fluid flow direction as a result of their interaction with the other particles in the bed (Wang, et al., 2009).

Above the fluid threshold constant saltation occurs while a particle supply is available. Once developed, a saltation cloud can be maintained by wind speeds lower than the fluid threshold, as the bombardment of saltating grains ejects other particles. This lower wind speed is referred to as the *impact threshold* (Bagnold, 1941). The variation between fluid threshold and impact threshold for various particle diameters is illustrated in Figure 1-5. The relationship applies best to homogeneous particle size distributions, or very well sorted unimodal distributions. For a poorly sorted particle size distribution, including bi-modal and tri-modal distributions, it is possible to exceed the impact threshold only for smaller diameter particles while larger diameter particles are limited either to creep or to remaining stationary.

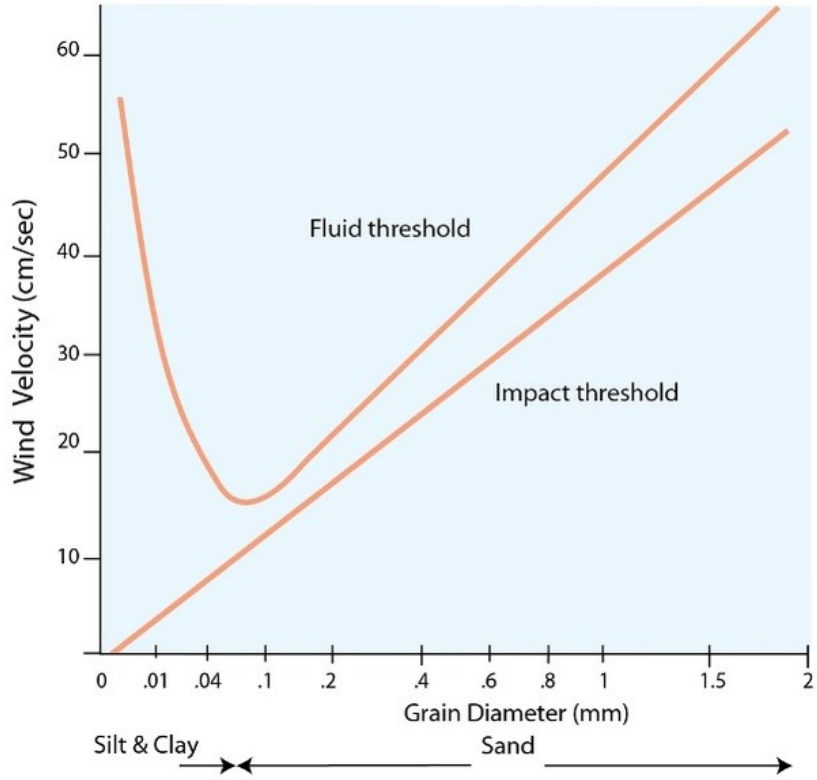

Figure 1-5 Fluid and impact thresholds for particles in an air flow (after Bettis III, 2012)

1.3 Aeolian Impact Ripples

Surface irregularities affect the spatial distribution of impacts from saltating grains resulting in areas of higher and lower numbers of impacts, as shown in Figure 1-6. The variation in the impact density results in the development of proto-ripples, with crests aligned perpendicular to the wind. Proto-ripples lack a defined wavelength, and are inconsistent in amplitude (Lancaster, 1995). Under continued bombardment, the proto-ripples grow in amplitude and develop a wavelength, becoming impact ripples (Greeley & Iverson, 1985). The saltation of finer particles results in the creep of coarse particles to the crest where they pile up, continuing the growth of the ripple height. As the ripples project higher into the air flow, the crest particles experience increased fluid drag. A critical point

is reached when the crest particles are either entrained in saltation, or transported off the crest as creep load. It is therefore the size of the coarsest particles in combination with the wind speeds that limits the height of impact ripples (Greeley & Iverson, 1985; Lancaster, 1995).

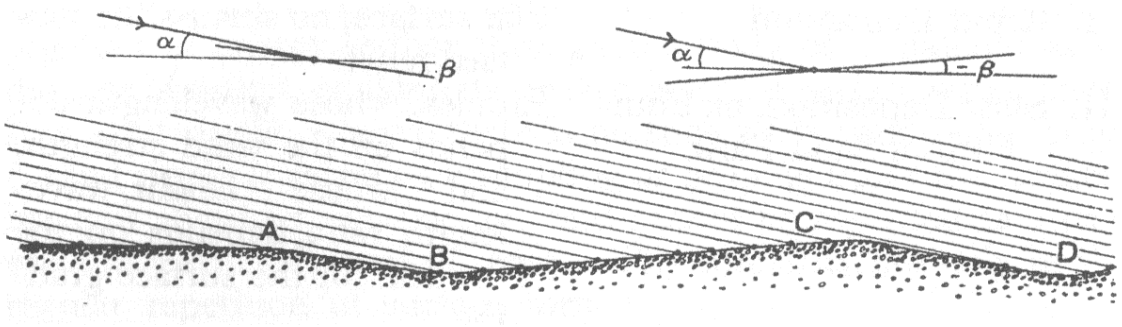

Figure 1-6 Illustration of the effects of minor topographic variation on saltation flux density. The area B to C receives more impacts than area A to B, owing to local variation in surface slope. As a result areas of the sand bed experience preferential erosion, B to C, or sheltering, A to B (after Bagnold, 1941).

Aeolian impact ripples exhibit remarkably consistent amplitude and wavelength, both in the field and in wind tunnel experiments. Bagnold (1941) predicted ripple wavelengths when observing a kink in the velocity profile during saltation. Attributing this kink to the top of the saltation cloud, he described the *characteristic saltation path* (Bagnold, 1941). He reinforced this concept with the finding of a high correspondence between wavelengths observed in his wind tunnel, and those he had calculated using the characteristic saltation path length (Bagnold, 1941). Sharp (1963) challenged the work of Bagnold based on field studies in California which showed that under steady wind speed, ripple wavelengths increased with time. Sharp (1963) proposed that while the mean saltation path is proportional to the wind speed, reptation and creep distances over time are not, and therefore the wavelength is not directly dependent on the mean saltation length. He proposed that reptation, not saltation, is the key transport mode that determines the wavelength of ripples.

The models of Bagnold and Sharp were further refined by Anderson (1987), who incorporated two populations of particle trajectories. He modelled a group of high-energy, low-angle particles undergoing saltation, and a group of low energy reptators. Anderson determined that the reptating population comprises the majority of the mass transport, and found that the mean wavelength of impact ripples corresponds with six to seven times the mean reptation length (Anderson, 1987; Pye & Tsoar, 1990). The experimental wind tunnel work of Seppälä & Lindé (1978) and Walker (1981) is in good agreement with Anderson's model results.

Ripple wavelength, λ, and amplitude, A, tend to increase with increasing wind velocity (Bagnold, 1941; Greeley & Iverson, 1985). Increasing mean particle diameter also tends to increase both λ and A (Bagnold, 1941; Greeley & Iverson, 1985). These relationships apply best to homogeneous or very well sorted unimodal particle size distributions. Wavelength and ripple amplitude tend to increase as the source particles become more poorly sorted, although this is commonly not the focus of experimental wind tunnel work.

1.4 Aeolian Megaripples

1.4.1 General Characteristics

Aeolian megaripples, also known as ridges, giant ripples, granule ripples, sand ridges, or pebble ripples (Greeley & Iverson, 1985), fall along the continuum of aeolian impact ripples (Lancaster, 1995, pp. 40, fig 2.19). Megaripples have bi-modal or tri-modal particle size distributions, in which the coarsest mode is generally three to seven times the diameter of the finer mode ($3 < d_c/d_f < 7$) (Bagnold, 1941). Unlike small aeolian impact ripples where

all particles can be entrained by the flow, the coarsest particles in the size distribution are generally limited to creep. This segregation of transport mode by particle size is believed to be fundamental to megaripple formation (Isenburg, et al., 2011). If $d_c/d_f > 7$ a deflationary lag surface (*desert pavement)* forms as the saltation cloud has insufficient energy to drive the creep required for crest formation (Pye & Tsoar, 1990). Megaripples are often classified as a form of lag surface, because of the surface coarsening and the fact that they only form under either equilibrium or deflationary conditions (Pye & Tsoar, 1990).

Megaripple bedforms have been documented in Iceland, Northern Canada, Antarctica, Israel and Argentina. The latter of these locations arguably contains the largest set of megaripples, with amplitudes of 2.3 m and wavelengths of 44 m (Milana, 2009; Milana, et al., 2010). Formed from large diameter, low density, volcanic pumice, these megaripples are located on a high altitude plateau where monitoring stations have recorded extreme winds of over 350 km hr^{-1} (Milana, 2009; Milana, et al., 2010). While these megaripples exhibit the key characteristics of other field locations (unimodal wind regime, bimodal particle size distribution, and transport mode segregation), there is still debate in the literature as to whether these bedforms are truly aeolian megaripples, or whether they are a variant of a dune bedform (Isenburg, et al., 2011). Similarly, very large ripple variants on Mars are commonly called transverse aeolian ridges, or TARs (Yizhaq, 2005). Further study of these bedforms is required to provide definitive classification.

Many writers have noted that sufficient time is required to produce large bedforms. Bagnold (1941) originally hypothesized that the megaripples he observed in the Libyan Desert would take decades or centuries to form. Sharp (1963) found in the Kelso Dunes area of California that the sand was reworked into megaripple forms in only weeks during intense wind storms. Sakamoto-Arnold (1981) reported that it is possible for small

megaripple bedforms to develop in just days or hours given a sufficient supply of coarse particles to rework. Megaripple evolution has been observed to attain equilibrium within a time frame of one to two years in the Nahul Kasuy region of Israel (Isenburg, et al., 2011), illustrating that the evolution of megaripples appears to be highly site specific owing to the complexity of environmental variables involved.

The typical bimodality of the particle size distribution is displayed in samples from the Nahul Kasuy region of Israel as shown in Figure 1-7. Creep, which is driven by the saltation of the finer mode of particles, results in the accumulation of coarse particles on the crest of the ripples. The characteristic placement of the coarsest particles on the crest with fine particles in the trough was also noted by Sharp (1963), where coarse particles comprised 50-80% of the crests, but only 10-20% of the troughs.

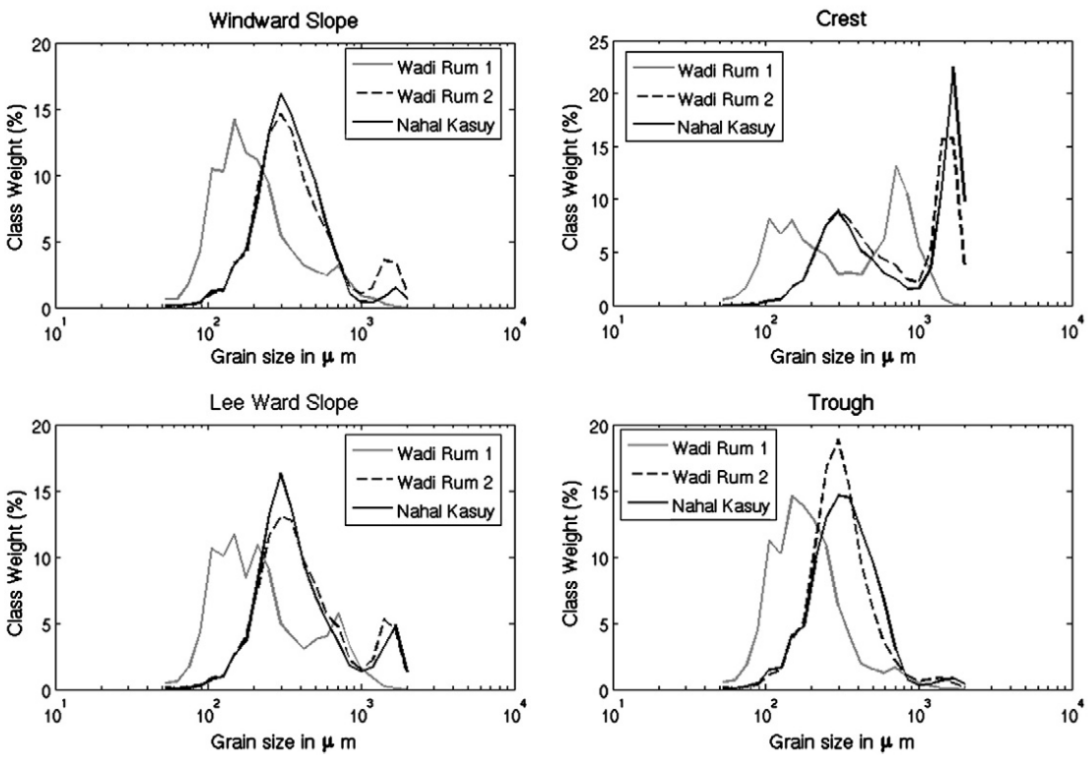

Figure 1-7 Particle size distributions for three megaripple fields illustrating variation along a wind aligned transect. Note the distinctly higher concentration of coarse particles on the crest versus the troughs (after Isenburg, et al., 2011).

As previously mentioned, most megaripples are composed of particles of similar parent material; Greeley & Peterfreund (1981) report on an interesting set of megaripples in Iceland that deviates from this norm. The particle size distribution consists of small diameter, high density obsidian and large diameter, low density pumice. The resulting bedform has dark crests composed of obsidian, and light coloured troughs composed of pumice. This example illustrates that particle mass, as determined not only by volume but also by density, is a determining factor in the threshold limits of motion. The arrangement of particles within the Iceland megaripples is consistent with the findings of Gerety & Slingerland (1983), in which thresholds of motion were determined for mixtures of similar diameter particles from quartz, garnet, and olivine sources. The conclusion of Gerety & Slingerland (1983) was that transport models which incorporate average densities are unable to account for size-density variation within a sand bed. Particular care must be taken when modelling sediment transport for a particle size distribution that contains multiple mineral sources.

In Isenburg et al. (2011), the evolution of megaripples was studied by levelling portions of the desert surface. Stereoscopic imagery was utilized to create digital elevation models (DEM) of the pre-existing megaripples, the surface after levelling, and of the reformation of the ripples at varied time intervals. It was found that while impact ripples formed quickly after the surface was levelled, wind direction changes resulted in the reworking of the surface. Pye and Tsoar (1990) suggest that a deviation of greater than 20° of the incident wind direction will result in the realignment of impact ripple crests. Isenburg et al. (2011) observed that megaripple bedforms required roughly two years to completely redevelop, thus illustrating this long term dependency on unimodal wind regimes of the region. Large aeolian megaripples exhibit a higher degree of horizontal

symmetry than typical impact ripples, and this is believed to be caused by wind variations over the long time required for their growth (Lancaster, 1995).

The conditions of segregation by transport mode (i.e. fines in saltation/reptation, coarse limited to creep) is reinforced by findings from a field study in which megaripple bedforms were studied under high intensity wind storms (Isenburg, et al., 2011). When the wind forces exceeded the impact threshold for the coarsest mode of particles in the distribution, the entire sand bed underwent saltation and reptation. These events led to the flattening of the megaripples into a planar bedform (Isenburg, et al., 2011).

While the basic sediment characteristics and environmental conditions are known for the formation and evolution of megaripples from field work, there are few experimental studies reported in the literature (Manukyan & Prigozhin, 2009). Bagnold created "ridges" in his tunnel from test beds having a bimodal particle size distribution (Bagnold, 1941 Fig. 51). Fryberger & Schenk (1981) used particles gathered from a megaripple field in an attempt to recreate the bedforms within a wind tunnel. Other than these two examples, the focus within the literature has been on the field studies previously mentioned, as well as on numerical modelling exercises, and more recently on development of cellular automaton models (CAM).

1.4.2 Numerical Modelling and CAM projects

Owing to the time frame for the typical development of large megaripples, numerical models and CAM projects are powerful tools for understanding the evolution of these bedforms. Additionally, these experiments can help to understand the influence of system

variables, such as wind speed or particle size distribution, through controlled alteration of sediment transport dynamics.

Building on previous impact ripple models, Yizhaq *et al*. (2004) present an analytical model specific to bimodal sand beds, which was developed by combining field observations of ripple morphology with meteorological data. The model incorporates a "phenomenological parameter", ε, which corresponds to the proportion of fine mode particles present at a given location on the bed surface. A value of $\varepsilon = 1$ represents equal fine mode to coarse mode proportions, while $\varepsilon = 0$ represents only fine mode particles. It is important to note that the localized proportion of fine or coarse mode particles cannot exceed that of coarse particles within this model. Simplifications are made with regard to the particle sizes and the environmental conditions, specifically, the particles are assigned spherical shapes and identical densities, and wind speeds are steady and uniform. The model is able to create bedforms that exhibit the general morphometric characteristics of megaripples observed in the Nahul Kasuy region of Israel. The deficiency of this model is the lack of strict segregation of transport modes, and the limitation placed on the localized particle mode concentration.

Yizhaq (2005) presents the results of the model from Yizhaq *et al*. (2004) when applied to transverse aeolian ridges (TAR) found on Mars. Modifications are clearly required to accommodate the differences in atmospheric composition, gravitational properties and sediment characteristics. To further complicate the matter, TARs are still lacking clear classification as either impact ripple or dune bedforms, falling into a similar category as that of the large megaripples of Argentina (Yizhaq, 2005). The assumption is made that the mechanism for megaripple creation (the accumulation of coarse mode particles on crests) is the same as that on Earth. The model is unable to account for the

large size of the TARs found on Mars, although the author states that a larger spatial domain and more computational time is required to gather more information (Yizhaq, 2005). The continued development of numerical models, validated against both field and experimental data, will greatly increase our ability to understand not only aeolian systems on Earth, but also on planets such as Mars, Venus and Saturn's moon Titan.

A numerical model designed to address the characteristics of megaripples is presented by Manukyan & Prigozhin (2009). Aiming to address a deficiency of previous models, such as transport mode segregation, the model incorporates a heterogeneous particle size distribution. The model differentiates the two modes, coarse and fine, limiting the coarsest mode to creep. While the model presented in Manukyan & Prigozhin (2009) is able to simulate bedforms that match morphometric measurements obtained from field sites and to model the surface sorting of particles, as shown in Figure 1-8, numerous assumptions are made for parameterization of the model. It is clear that the model predicts coarse particles on the surface of the crests, with fine particles comprising the troughs.

In many instances it is made clear that the model is only able to provide limited results, as there are insufficient experimental data available for validation. The authors state clearly that "*available experimental data on aeolian transport are scarce and we tried to make a reasonable choice of model parameters guided also by the results of numerical simulations and our limited theoretical understanding...*" (Manukyan & Prigozhin, 2009, pp. 031303-6).

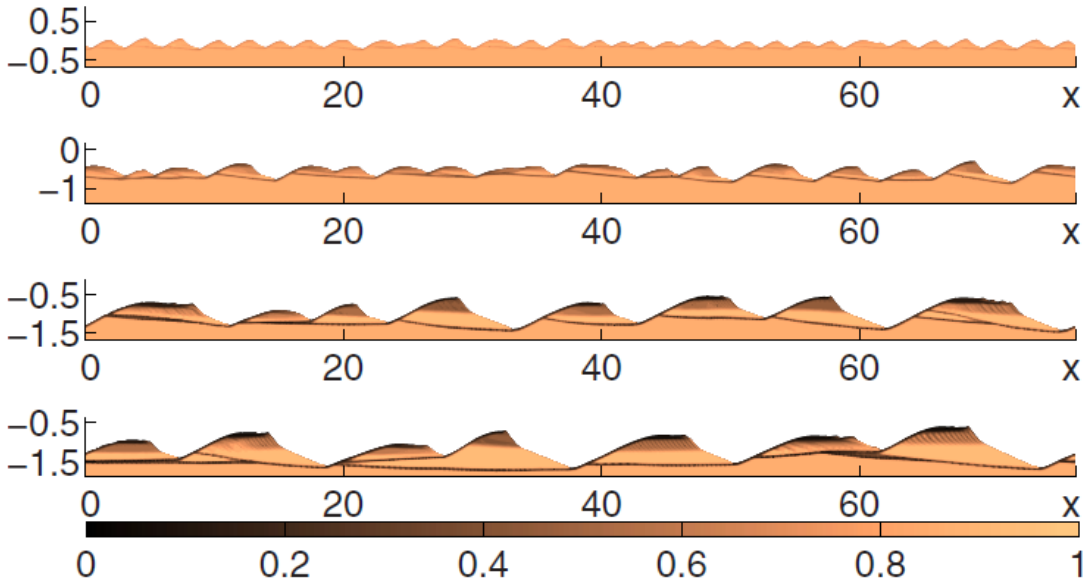

Figure 1-8 Surface sorting modelled for ripples as a time series. From top to bottom, T=0.3, 1.7, 5.6 and 13.5hrs. Colour bar indicates local proportion of fine mode particles. A clear separation of fine mode and coarse mode particles is exhibited between trough and crest (after Manukyan & Prigozhin, 2009).

Numerical modelling, when integrated into a cellular automaton framework, can further reveal information about the sensitivity of bedform evolution to model parameters. The most recent and sophisticated CAM project is outlined in Eastwood et al. (2011). Variation of the sediment supply and the transport capacity, for example, allows for the production of aeolian bedforms that resemble those found on both Earth and Mars, including ridges, barchan dunes, and superimposed dunes (Eastwood, et al., 2011).

Even with the advancement of numerical models and CAM projects, there remains a fundamental lack of experimental data, as required for validation and calibration. Addressing megaripples specifically, Isenburg et al. (2011, pp. 70) state "*basically, it is still not known whether megaripples continue to grow indefinitely or whether they reach saturation, and how the interplay between wind and grain size distribution dictates the wavelength.*" To further the point, Yizhaq (2008, pp. 1377) adds, "*wind tunnel experiments*

could help investigate megaripple evolution in sands with different bimodal grain-size distributions and different wind speeds."

1.5 Core Objectives

The statements above have guided the core objectives of this research which will address fundamental questions regarding the influence of particle size distribution and wind speed on the morphometrics of impact ripples created in sand of varied textures.

1) Determine the influence of wind speed on impact ripple morphometrics for sand beds of varied textures.
2) Determine the influence of particle size distribution on impact ripple morphometrics for sands of varied textures.
3) Investigate surface sorting of coarse and fine modes of particles within impact ripples for sands of varied texture.
4) Investigate the process of spatial organization and its relationship to the development of impact ripples in sand beds of varied texture.

To accomplish the objectives of this research, new digital techniques will be developed for the analysis of sand beds utilizing particle tracer technologies. By systematically defining the morphometric influence of wind speed and particle size distribution, this study will provide both the field research and numerical modelling communities with valuable information.

Chapter 2 Methodology

2.1 Methodology Overview

Sand samples were created using naturally beige sand and dyed red sand. Sieving eliminated any overlap in size, producing two distinct populations with colour distinguishing size. Five sand beds with varied proportions of red to beige particles were subjected to four freestream velocities within the Trent Environmental Wind Tunnel Facility. Velocities exceeded the fluid threshold for the beige particles, but not the impact threshold for the red particles. For each particle size distribution and wind speed combination, topographic data were collected as a time series with a non-contact 3D digitizer. Additionally, optical data were collected as a time series with a digital camera. The topographic data were analysed by means of digital elevation models to extract morphometric indices. The optical data were processed using colour classification to explore the spatial distribution of the coarse red particles.

2.2 Trent Environmental Wind Tunnel Facility

The Trent Environmental Wind Tunnel is a suction type tunnel located within a climate chamber. Temperature in the lab can be set within the range of -10 °C to 40 °C with ±0.1 °C precision. Humidity is measured as relative saturation, and is adjustable within the range of 5 % to 95 %, with ±2 % precision. More detail on the climate control system can be found in McKenna Neuman (2003, 2004). Variable pore water tension can influence the cohesion of particles, and alter the fluid threshold for a sand bed (McKenna Neuman, 2004), so to minimize any such effect, the facility was maintained at 19.0 °C and 30 % relative humidity for all test runs.

The facility has an open intake and is capable of free stream wind speeds ranging up to 20.0 m s^{-1}. The intake area has a contraction bell with a two dimensional compression ratio of 2.5:1 (McKenna Neuman & Maljaars, 1997), and a flow straightening array to minimize turbulence within the air intake. The working section of the tunnel is 13.8 m long, the entire tunnel being 19.1 m in length. The tunnel is rectangular in cross section - 0.76 m tall and 0.71 m wide, or 0.54 m^2 in cross sectional area. Detailed descriptions of the tunnel facility can be found in many published works that have utilized the facility (McKenna Neuman & Maljaars, 1997; McKenna Neuman, 2003; McKenna Neuman, 2004).

A trip plate consisting of 2.5 cm high by 1.9 cm diameter dowels placed with 4.5 cm centre-to-centre spacing in staggered rows, initiates the development of a boundary layer (McKenna Neuman & Maljaars, 1997). This plate is located directly downwind of the contraction bell.

2.3 Sand Sample Preparation

The bimodal test sand beds were created from two sources, quartz particles which are naturally beige and feldspar particles that are dyed red. The quartz particles, industry grade #55, are derived from beach sand; they exhibit high sphericity and rounded grains (Pye & Tsoar, 1990). The particle size distribution is near normal, as shown in Figure 2-1.

The red feldspar particles, industry grade #16, are created by crushing pure feldspar, sieve sorting, and then dying within a rotating drum. Feldspar, when crushed, produces elongated, platy particles (Pye & Tsoar, 1990); the dying process rounds the particles, resulting in similar physical characteristics to that of the quartz used. The particle shape characteristics of the two groups are shown in high resolution in Figure 2-2. The particle size distribution for the red feldspar is near normal as also shown in Figure 2-1.

Quartz and feldspar are of comparable density, quartz being 2650 kg m^{-3} and feldspar being 2560-2700 kg m^{-3} (Pye & Tsoar, 1990), their densities are therefore considered to be the same for the purposes of this research.

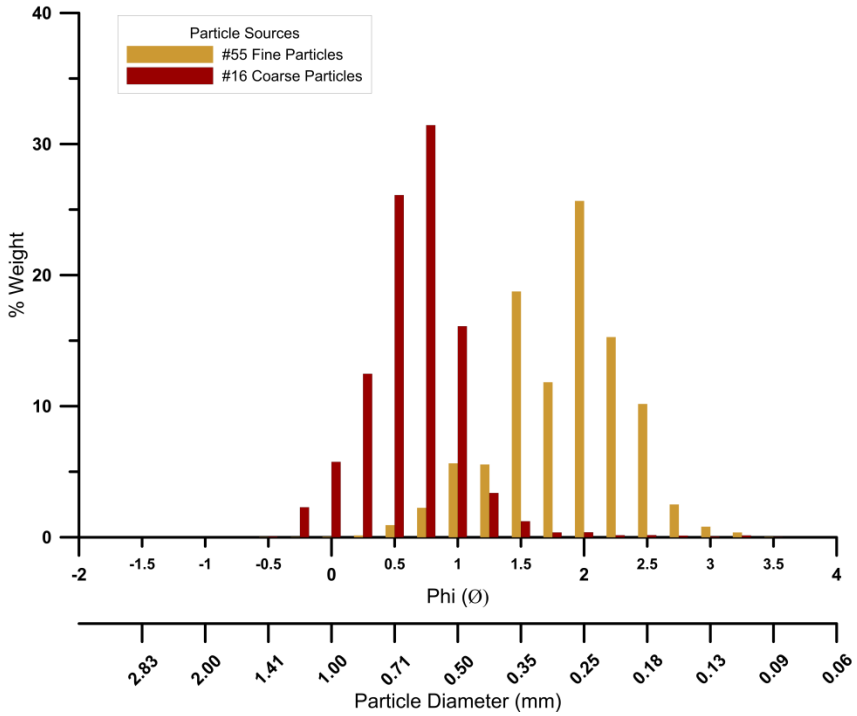

Figure 2-1 Particle size distribution for #55 and #16 sands.

Figure 2-2 Close up photograph of mixed sand bed illustrating particle shape characteristics, including the similarity of coarse and fine particle shape

The two particle groups were filtered through a sieve with a 542 μm nominal opening. Beige particles that passed through the sieve were retained, while red particles that failed to pass through the sieve were retained. This process produced a population of beige particles finer than 542 μm, and red particles coarser than 542 μm. The beige particles were used to represent the fine mode, while the red particles represented the coarse mode. The use of a 542 μm sieve versus 500 μm, which corresponds to the Wentworth classification for coarse sand, is attributed to the limited availability of screen. A custom 40 cm diameter sieve was constructed to process more than 600 kg of sand used in this research.

The two particle populations were mixed in known proportions to create the five sample sand beds. Particle size analysis with ¼ phi sieves was conducted to determine the percentage of coarse mode particles (red) by mass ($\%_C$). The cumulative particle size distribution (PSD) of each sample is shown in Figure 2-3, with summary information in Table 2-1. A detailed histogram style PSD for Sample 2 is shown in Figure 2-4, to aid in visualizing the two colour groups.

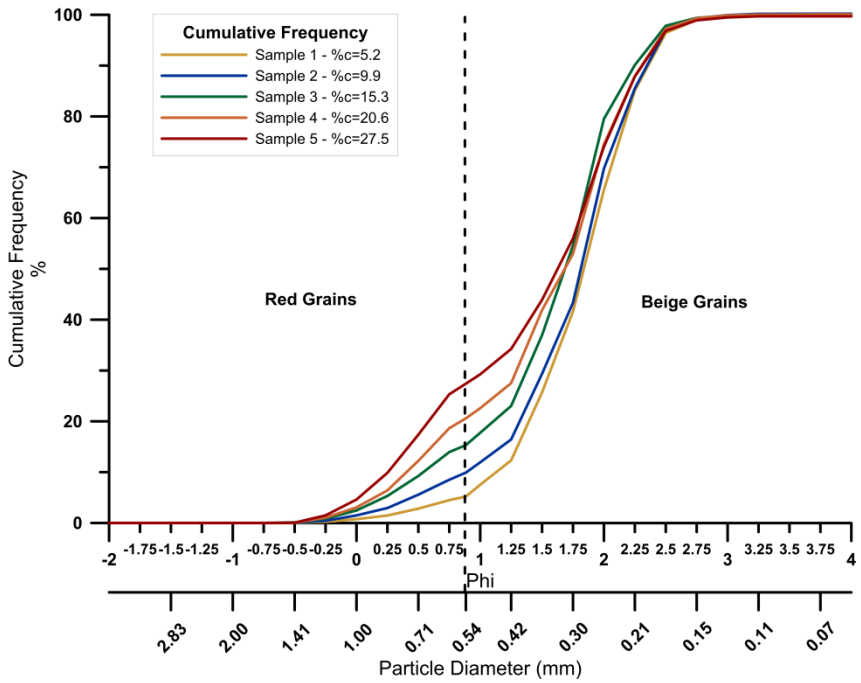

Figure 2-3 Cumulative frequency particle size distribution for all samples illustrating variation of coarse mode proportions

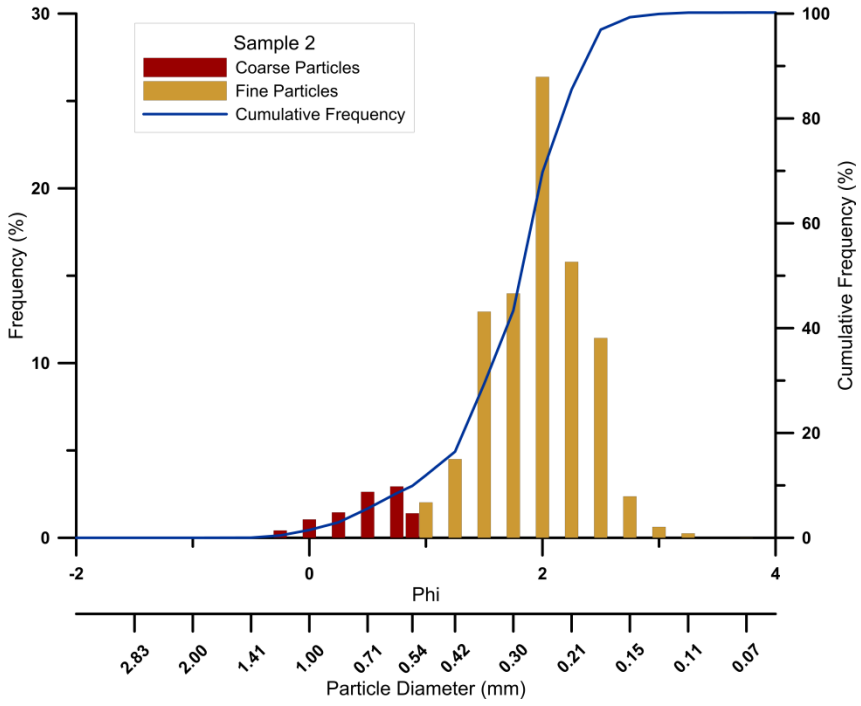

Figure 2-4 Particle size distribution for Sample 2, illustrating fine and coarse mode particles and their corresponding colouration.

Table 2-1 Summary table of particle size characteristics

Sample Name	Percentage Coarse by Mass $\%_C$	d_{50} (mm)
Sample 1	5.2	0.289
Sample 2	9.9	0.311
Sample 3	15.3	0.350
Sample 4	20.6	0.368
Sample 5	27.5	0.399

2.4 Test Bed Preparation

Pilot studies showed that the initiation of sand ripples for these sand beds requires either deflationary or equilibrium conditions, which is consistent with existing literature. It was found that utilizing the entire working section of the tunnel caused accretion conditions beneath the measurement window. To ensure a deep turbulent boundary layer, 19 mm crushed stone was placed sparsely for 305 cm of the tunnel, downwind of the dowelling trip plate, shown in Figure 2-5 . The sand bed began at the end of the sparse stone, as shown in Figure 2-6, and consisted of 430 cm of sand upwind of the measurement window, then an additional 100 cm of sand downwind of the measurement window. Extension of the sand bed past the measurement window ensured continuity of the sediment transport and airflow conditions past the measurement window.

Figure 2-5 Transition from wooden dowelling to sparse stone.

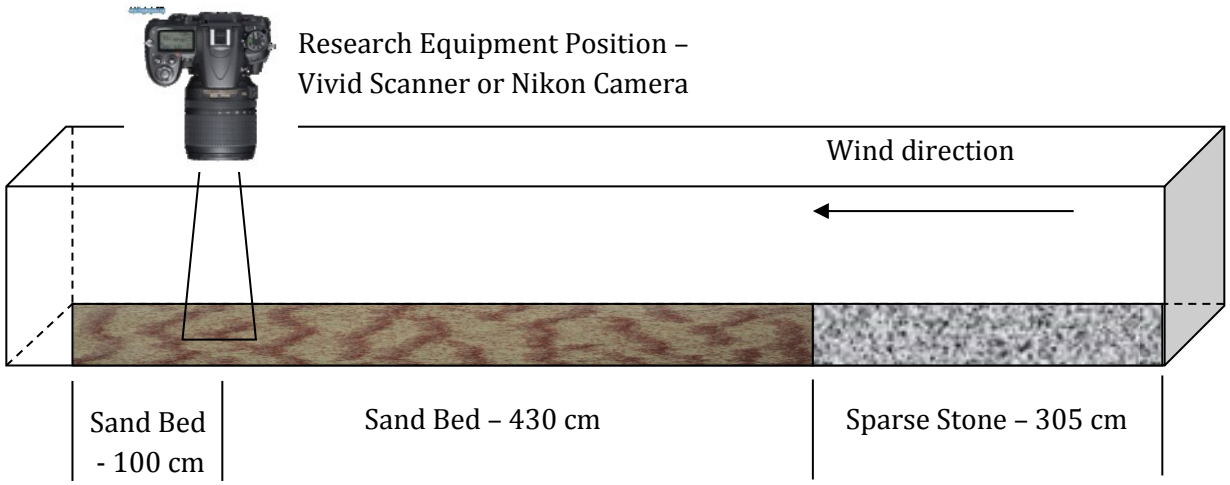

Figure 2-6 Schematic of test bed configuration (not to scale).

The sample sand beds were set up by first mixing the sands in a cement mixer to ensure a uniform distribution of particles throughout the sample, and by remixing between each test run. The sand was placed in the working section of the tunnel, and levelled to a depth of 38 mm. This procedure has been utilized in previous wind tunnel studies within the Trent Environmental Wind Tunnel (Gordon & McKenna Neuman, 2011; McKenna Neuman & Maljaars, 1997; McKenna Neuman, 2003).

2.5 Wind Speed Selection

To emulate the conditions in which megaripples are known to form, wind speeds used in this study exceeded the fluid threshold for the fine mode particles, yet did not exceed the impact threshold for the coarse mode particles. Determining the range of appropriate wind speeds required two separate methodologies.

2.5.1 Fluid Threshold Testing

The fluid threshold for the fine mode, the beige particles, was determined using a strip of the test sample 11.5 cm wide, 835 cm long, and 3.2 mm deep. The sample began at the terminus of the roughness plate (the sparse stone was not present), and extended beyond a Wenglor ZD600PCVT3 sensor, mounted such that its beam was aimed across to the particle strip. Saltation is a cascading process, thus requiring a long fetch. The Wenglor sensor samples interruption of the beam at 100Hz; its output was logged with a CR-3000 data logger and averaged into 0.1 s bins. The data were further converted to cumulative counts and plotted as a time series, as shown in Figure 2-7.

To ensure that the threshold velocity determined was not skewed by perched particles, once threshold was reached, the wind speed was reduced and the test repeated. Threshold was determined on the graph as a wind speed at which the cumulative counts continued to increase steadily, and not level off, as indicated by the dashed line on Figure 2-7. The fluid threshold was quantified within a 0.25 m s^{-1} range with this setup, sufficient for the requirements of this research project. Threshold values for the various sample beds can be found in Table 2-2.

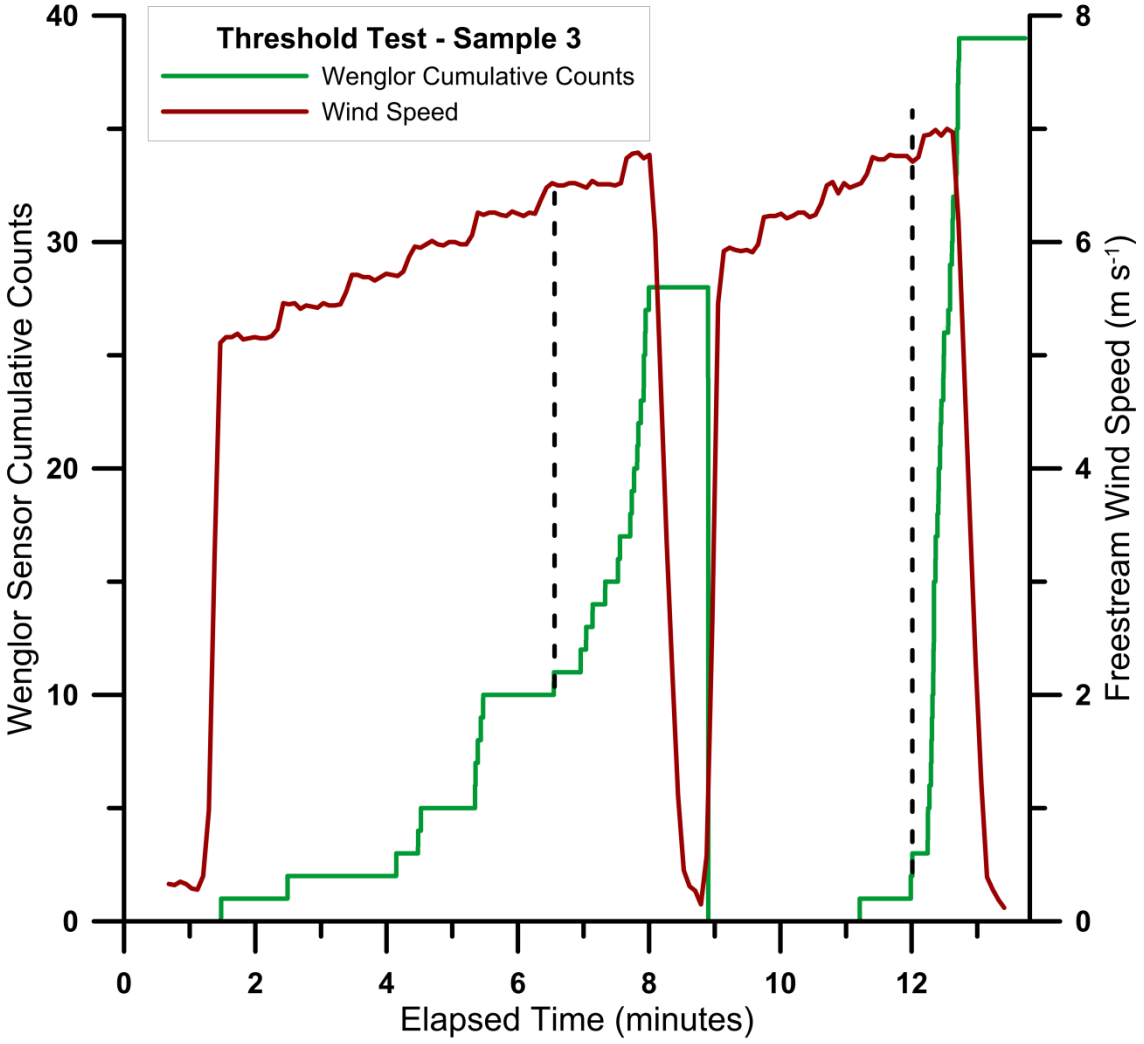

Figure 2-7 Threshold testing plot for Sample 3 illustrating the correlation of cumulative wenglor counts to the wind speed. Dashed line indicates fluid threshold wind speed. Test was repeated twice to allow perched surface particles to be removed during the first instance. Second test measures threshold for an adjusted surface.

Table 2-2 Fluid threshold velocities (m s^{-1}) for the sample beds

Sample Name	Percent Coarse by Mass	Fluid Threshold
Fine (Beige) only	0.0	5.75 – 6.00
Sample 1	5.2	6.00 – 6.25
Sample 2	9.9	6.00 – 6.25
Sample 3	15.3	6.50 – 6.75
Sample 4	20.6	6.50 – 6.75
Sample 5	27.5	Not tested
Coarse (Red) only	100	12.75 – 13

2.5.2 Impact Threshold for Coarse Mode Particles

The impact threshold for the coarse mode was determined by suspending a trap above the sand bed to catch saltating grains. The bottom of the trap mouth was placed 7 mm above the surface of the test bed, with the area directly below the trap secured with spray adhesive to ensure that unwanted erosion did not occur. The placement at 7 mm was the closest physically possible, and placed the opening within the saltation cloud. A photograph of the trap setup is shown in Figure 2-8.

Sample 1 ($\%_C$ = 5.2) was utilized for this test and was subject to air flows at varied speeds for 1 minute intervals. The wind speed was increased in 0.5 m s^{-1} increments, with the trap being emptied and the contents collected between tests. The sediment collected was visually inspected for the presence of red grains. The impact threshold for the coarse, red grains within Sample 1 is in the range of 12 to 12.5 m s^{-1}, which corresponds to roughly 90% of the fluid threshold as determined for Sample 1.

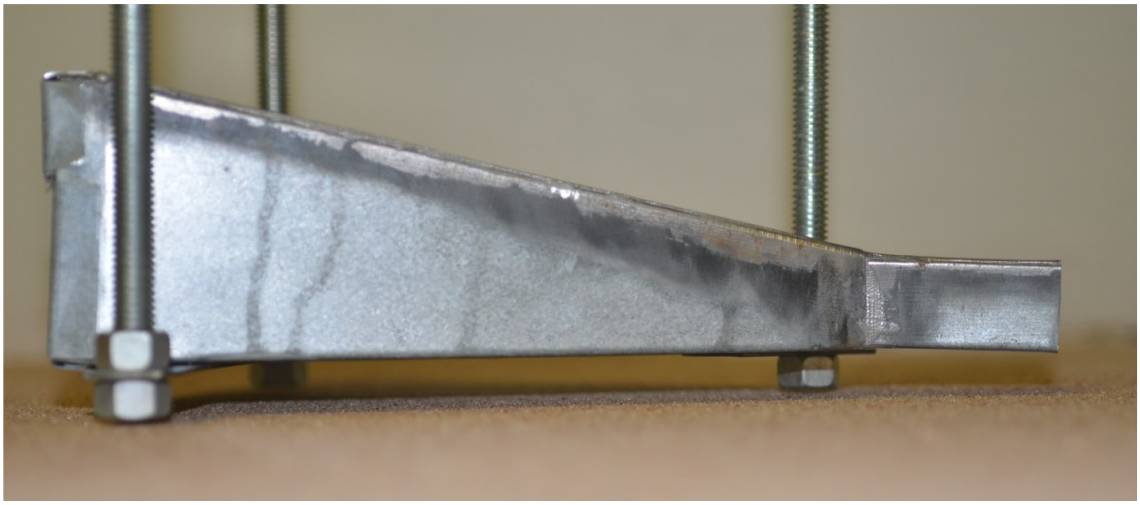

Figure 2-8 Hanging trap placement for capturing saltating grains within the wind tunnel

2.5.3 Experimental Wind Speeds

The above methodology guided the decision to use four free stream wind speeds in this research – 8 m s^{-1}, 9 m s^{-1}, 10 m s^{-1}, and 11 m s^{-1}. Nominal free stream velocities were systematically 0.2 m s^{-1} lower than requested speeds, which yielded the experimental free stream velocities found in Table 2-3.

Table 2-3 Experimental freestream wind velocities

Nominal	Actual U_∞
8 m s^{-1}	7.8 m s^{-1}
9 m s^{-1}	8.8 m s^{-1}
10 m s^{-1}	9.8 m s^{-1}
11 m s^{-1}	10.8 m s^{-1}

A single test at $U_\infty \approx$ 12 m s^{-1} was conducted for Sample 4 and it was noted that a large number of red particles were able to escape the wind tunnel through the fan outlet, indicating that the coarse mode was indeed saltating.

For each of the sand samples, morphometric and optical data were collected at each of the free stream velocities. This resulted in eighteen combinations of wind speed (U_∞) and proportion of coarse mode by mass ($\%_C$). At least one replicate optical collection experiment was completed for each sand sample to assess repeatability of the results.

2.6 Morphometric Data Collection

The morphometric data set (Digital Elevation Models – DEM) was collectede with a Konica-Minolta Vivid 9i 3D non-contact digitizer, hereinafter referred to as the "Vivid". The Vivid was placed in a custom window in the top of the tunnel looking down at the sample bed, consistent with the setup shown in Figure 2-6. The Vivid scans a surface into a 640

column by 480 row data cloud and creates a DEM with vertical accuracy of ±0.01 mm (Konica-Minolta, 2004). The horizontal resolution is dependent on the distance of the sensor from its target, and with the given setup produced DEM data with a spatial resolution in the x direction (spanwise) of 0.701 mm/point, and 0.672 mm/point in the y direction (streamwise). The minor change in spatial resolution with deflation of the sand bed is considered negligible, and was further reduced by cropping data to the spatial extents of the initial scan.

To demonstrate the reliability of the Vivid, and to check for any irregularities, the same sand surface was scanned twelve consecutive times. The estimated standard deviation , in millimetres, at each of the nodes can be found in Figure 2-9, with over 95% of the data points having a deviation of less than 0.08 mm.

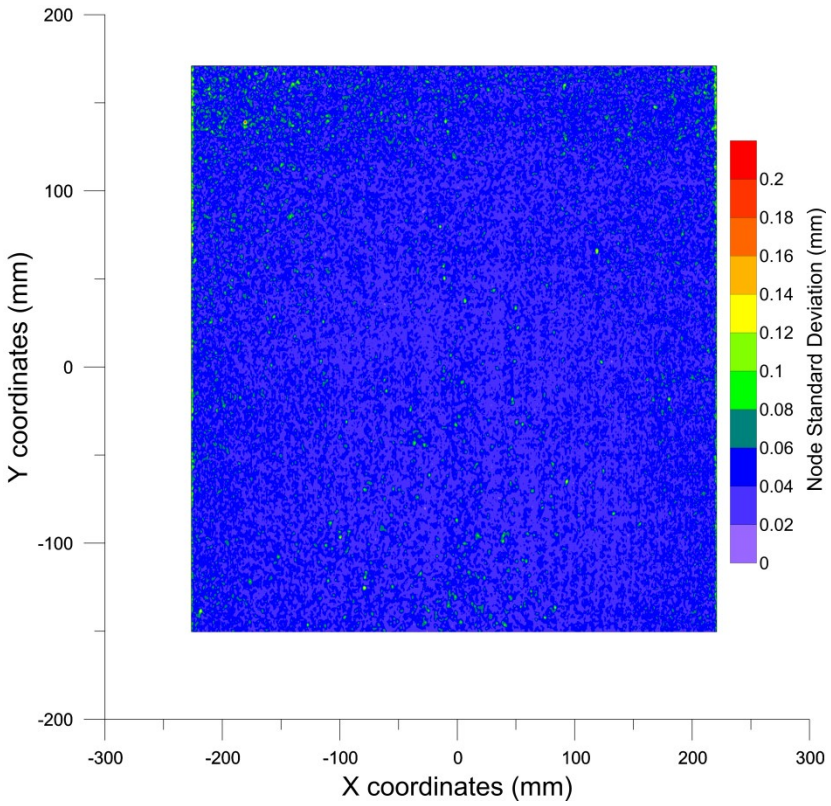

Figure 2-9 Node standard deviation for twelve consecutive scans of the same sand surface. It is evident that the average deviation at any given node is below 0.06 mm. Maximum variance is 0.2 mm.

The time required for a Vivid scan, roughly 2 minutes, requires that the tunnel be stopped in order to collect data for a rapidly developing bed form. A higher temporal resolution was utilized in the early phases of each test to capture the initial development of the ripples, with Table 2-4 outlining the temporal resolution of the entire scanning process. Each experiment (wind speed (U_∞) and proportion of coarse mode by mass ($\%_C$) combination), had morphometric information collected for these intervals.

Table 2-4 Topographic scan temporal resolution (all values in minutes)

Elapsed Time	Scan Interval
0 – 10	1
10 – 20	2
20 – 60	5
60 – 80	10
80 – 120	20

2.7 Morphometric Data Processing

The data clouds obtained from the Vivid scanner were converted into Golden Software Surfer® grid format, using Golden Software Scripter® and customized scripts. Code for the custom scripts is available in the digital appendix of this document. For a generalized flow diagram of the gridding process, refer to Figure 2-10.

Grids were created using the universal kriging interpolation algorithm. While this algorithm does not account for anisotropy in the data set, the number and density of data points is sufficient such that anisotropy does not greatly influence the final result (Golden Software Inc., 2012).

The full spatial resolution of the scanner was utilized when analyzing for mass loss fluxes. When analyzing the other morphometric indices such as amplitude and wavelength,

the high spatial resolution resolves individual facets of the largest particles, yielding slope values greater than 70°, which is beyond the expected angle of repose for sands. The data were therefore down-sampled to 2 mm spatial resolution, slightly larger than the largest particles of 1.4 mm diameter. The down sampled grid files contained 225 rows and 162 columns of data, totaling 36450 data points.

The Vivid represents elevations as negative values, and therefore scans were converted to represent the sand bed thickness by subtracting a scan of the bare tunnel floor. A centreline cross section extracted from the DEM was opened in Mathworks Matlab® to measure the following morphometric characteristics:

- Amplitude
- Wavelength
- Stoss length

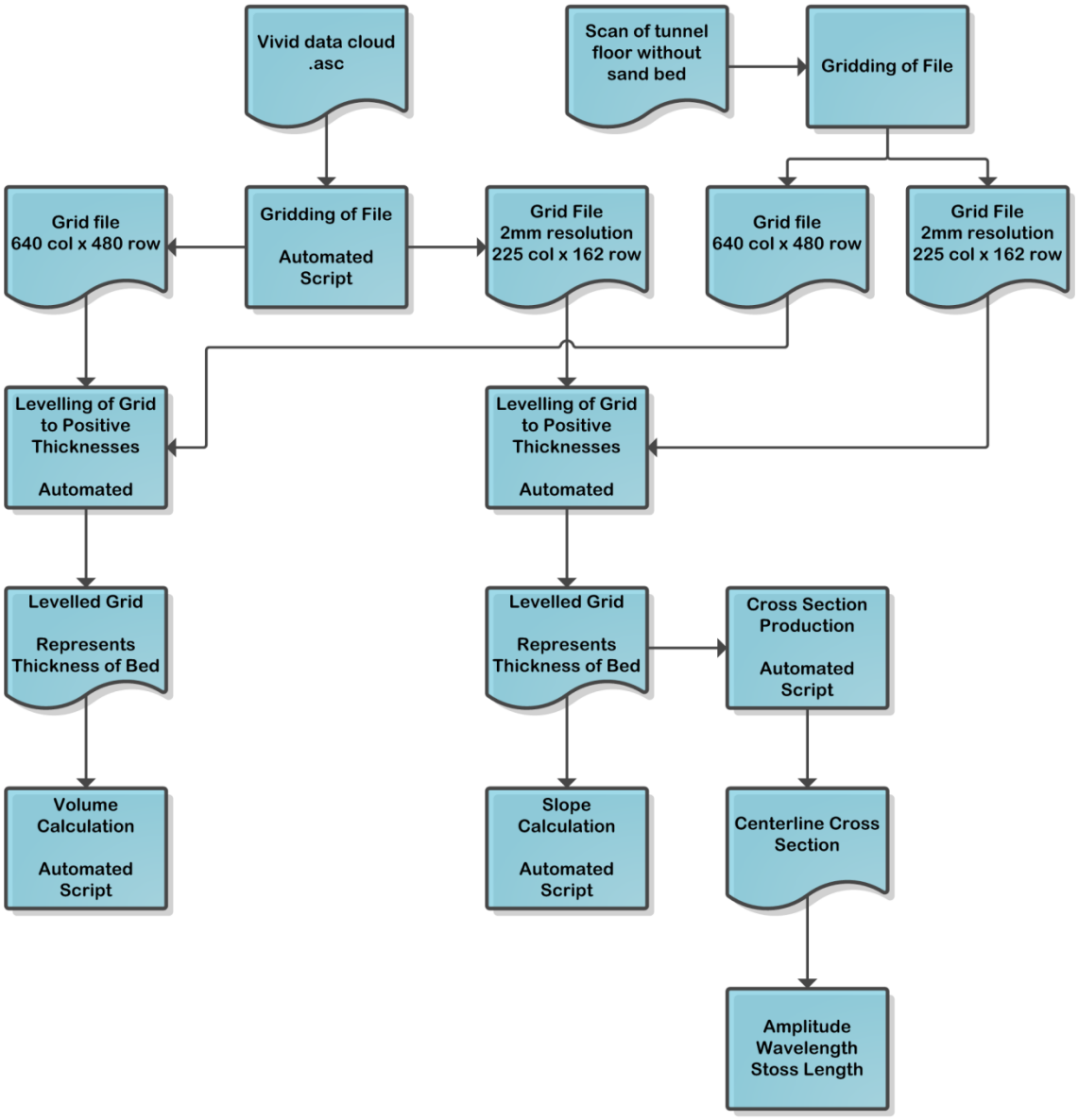

Figure 2-10 Morphometric data analysis flow chart

In most cases, more than one ripple appears in the cross section, so average measurements were made from at least three ripples. Ripple heights were manually measured from ripple peak to ripple trough using a data cursor. An example cross section is shown in Figure 2-11.

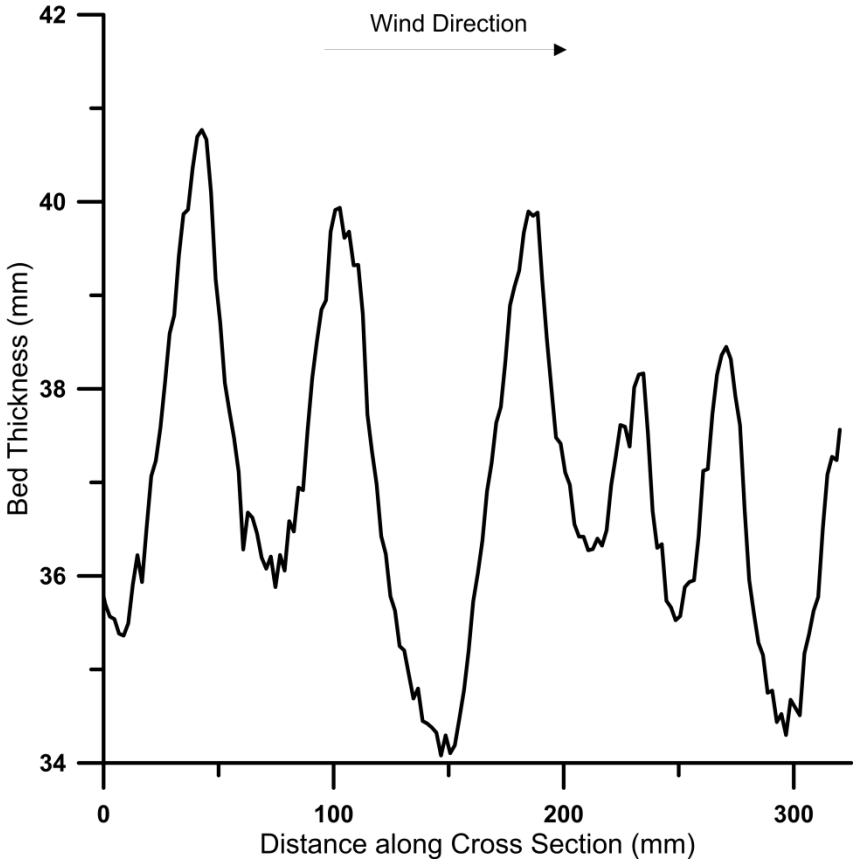

Figure 2-11 Cross section for Sample 3, wind speed 10 m s^{-1}, time 3000 s. Fifty five times vertical exaggeration to emphasize ripples.

Secondary morphometrics were calculated from the primary data, including the ripple index and the Ripple symmetry index. Ripple index is calculated as the ripple wavelength divided by the ripple amplitude. The ripple symmetry index is calculated as the horizontal ripple stoss length (trough to crest) divided by the ripple wavelength.

2.8 Optical Image Collection

The optical images for spatial analysis were acquired with a Nikon™ D7000 digital single lens reflex (DSLR) camera. The camera was mounted above the tunnel in the same position as the Vivid, consistent with Figure 2-6. It was fitted with a Sigma™ 50 mm macro lens, and viewed the sand beds through a custom built Lexan™ window. Applying the camera's digital multiplier to the lens focal distance resulted in an effective focal distance of 80 mm with a width to height ratio of 16:9. The camera was positioned such that wind direction travelled left to right in the images, allowing for the capture of more information in a streamwise direction as opposed to the spanwise. This configuration also prevented the capture of areas of the sand bed that may have been influenced by wall effects in the wind tunnel.

The lens had an F-stop of 2.8 which required the use of autofocus, as the deflation of the beds quickly led to blurry images if a fixed focal length was used. White balance was set manually to accommodate the fluorescent lighting of the laboratory, which was sufficient to provide contrast between the beige and red particles. The camera was leveled and aligned to the test bed prior to the start of each run.

The camera captures .JPEG images of 4928 x 3264 pixels which equates to 16 megapixels (MP), or 0.077 mm/pixel with the given setup. An interval timer setting allowed images to be captured every three seconds to a maximum of 999 images. Using this interval, a total image capture time of 50 minutes was possible. For each experiment (wind speed (U_∞) and proportion coarse mode particles by mass ($\%_C$) combination), this 50 minute time period was captured. In some instances, additional runs were conducted at 15 second intervals, equating to a 4 hour total run time.

2.9 Optical Image Data Processing

The goal of processing the optical images was to differentiate between the beige particles, representing the fine mode, and the red particles, representing the coarse mode. A custom Matlab® program was written to process the images, and the code is available in the digital appendix that accompanies this thesis. The .JPEG images were resized by a factor of 0.5 using the built in Matlab function *imresize()*, which takes the average of 4 x 4 blocks of pixels, known as bicubic down-sampling (Mathworks Inc., 2012). This reduced the computational processing time required and the loss of spatial resolution was negligible. The original spatial resolution was 0.077 mm/pixel, higher than the smallest expected grains within the sand bed.

2.9.1 Image Classification

The colour images were converted to L*a*b* (LAB) colour space for classification. This colour space, as opposed to Red Green Blue (RGB), differentiates luminosity from colour. The main advantage is that minor changes in lighting are negated, and colour values can be compared directly between images. Each pixel in the colour images is assigned a triplet, representing its luminosity, its position along the a* axis, and its position along the b* axis (Mathworks Inc., 2012). The a* axis is red through green, while the b* axis is blue through yellow, shown in Figure 2-12.

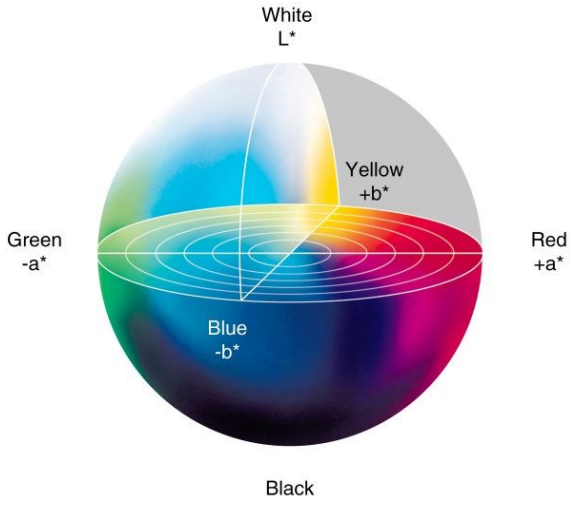

Figure 2-12 L*a*b* Colour space diagram

Matlab has built in functionality for conversion of colour space and image classification, and these functions were utilized in the process. The converted images were classified into two colour groups, using K-means clustering classification. K-means has a long history of use in remote sensing, and an excellent description and history is found in Jain (2010). To illustrate the k-means clustering process, classification for a single image is shown in Figure 2-13. It is shown that while a true separation in colour space does not occur, the differentiation along the a* axis is sufficient to separate the original image into two groups.

To ensure that the resulting images were represented consistently, the cluster group with the larger positive a* value was assigned a value of 1 (black), while all pixels in the other group were assigned a value of 255 (white). The binary images, representing presence/absence of coarse particles, were saved to an uncompressed .TIF image.

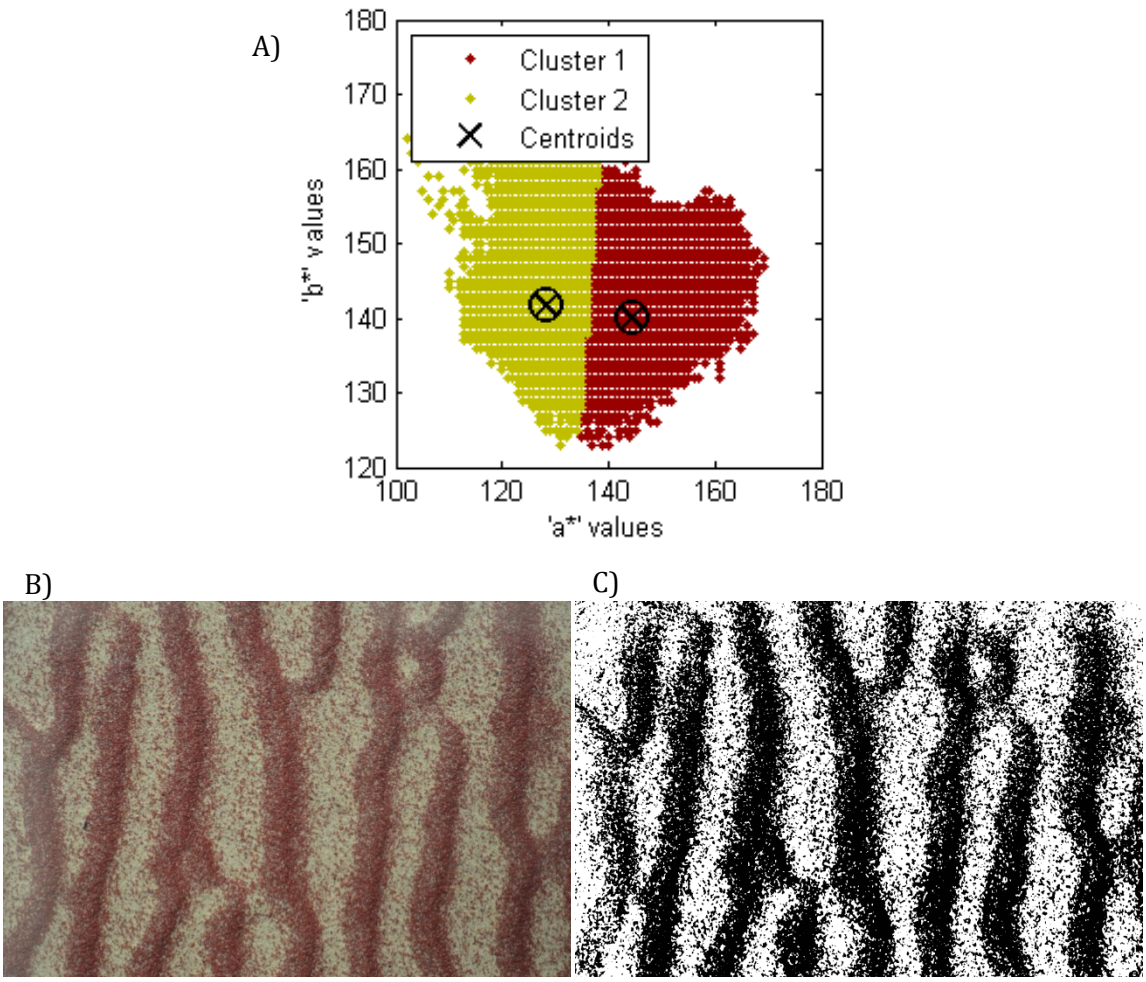

Figure 2-13 Illustration of k-means clustering algorithm results, showing A) separation in La*b* colour space, B) the original image, and C) the classified image.

Remote sensing software, such as ESRI ArcGIS or PCI Geomatica, also offers image classification algorithms in which the user can "train" the classification to distinguish specific spectral signatures; this method is known as supervised classification. The use of external software would have required the manual training of each of the 26 optical runs that were processed. The integrated nature of K-means clustering within the greater framework of Matlab significantly reduced data processing time.

2.9.2 Proportion of the surface represented by coarse mode particles β_C

The binary .TIF images representing presence/absence of coarse particles were used to determine the proportion of the bed surface area that was represented by the coarse mode particles - β_C. The built-in Matlab *find()* function was used for this process to determine the number of pixels with value 1, which was divided by the total number of pixels in the image. The proportion of the image composed of coarse grains was collected to investigate surface armouring, and to search for any relationships with ripple morphometrics.

2.10 Friction Velocity and Aerodynamic Roughness Length Measurement

Velocity profile data were collected with a Dantec custom laser Doppler anemometer (LDA). An excellent description of the LDA system is available in O'Brien and McKenna Neuman (2012). Air velocity data was collected in the streamwise and vertical directions at 26 logarithmically spaced vertical positions above the bed forms. The profiles began 3 mm above the bed form surface, and ended at 357 mm. The first two experiments had two profiles, one above the ripple crest and one positioned above the trough. Beginning with Sample 1 ($\%_C$ = 5.2) at U_∞ = 10 m s^{-1}, four vertical profiles were collected. Velocity measurement profiles were taken above the crest, leeward, trough and windward regions of the bedforms that developed during the optical data collection run, with example locations shown in Figure 2-14.

Minor migration of the bedforms occurred at the highest wind speeds, and this was accounted for during velocity profiling. Ripple migration rates were calculated from the topographic data obtained from a separate test run, and then incorporated into the

programmed positioning of the sample location, such that the sample was consistently taken above the same relative position. Migration rates were less than 1 mm min^{-1}; LDA profiling requires 20 minutes, so the motion of the bedform was accounted for.

While four profiles were collected over each bed, only the velocity profile above the ripple crest was used to calculate u_* and z_0, as this location is the least subject to bedform disturbance. The velocity profile data were plotted, and the Prandtl-von Karman equation (Equation 1-1) was used to solve for u_* and z_0, a common practice in aeolian studies. The Law of the Wall applies only to the bottom 10-20% of the boundary layer flow (McKenna Neuman & Maljaars, 1997), and therefore only the bottom 42 mm, or 15%, of the velocity profile was used in the calculations. A detailed study of flow characteristics above these bedforms is outside of the objectives of this thesis and remains a separate research endeavour.

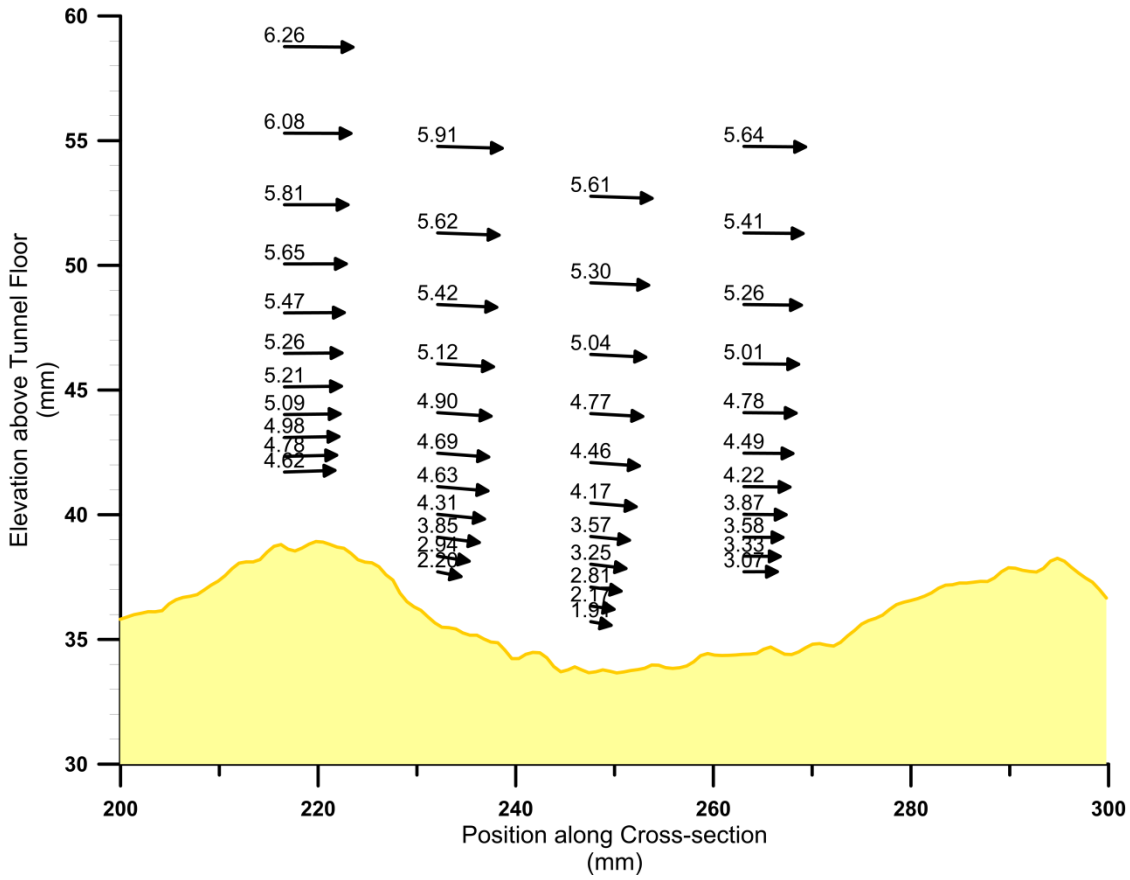

Figure 2-14 Velocity profile data illustrating data obtained at crest, leeward, trough, and windward sampling locations for Sample 2 ($\%_C$ = 9.9) at U_∞ = 9 m s^{-1}. All velocities in m s^{-1}.

Chapter 3 Results and Discussion

In total 26 wind tunnel runs were completed, covering 18 combinations of wind speed and particle size distributions. All particle beds were subject to 50 minutes of air flow, excluding Sample 1 at U_∞ = 11 m s^{-1}, as the high erosion rate was removed the entire thickness of the bed in 25 minutes. Samples 4 and 5 were in some cases exposed to a total of 4 hours of flow in order to determine if any meta-stable equilibrium change would occur. The values reported in all analyses refer to measurements obtained at 50 minutes into the experiment, unless otherwise specified. This allows for the comparison of both optical and morphometric data.

3.1 Mass Loss Measurements

The aeolian impact ripples examined in this study were intentionally created under conditions of net deflation, for the reasons outlined in the introductory chapter (§ 1.3, Page 8). Previous studies have discussed the need for deflationary conditions, including Bagnold (1941), and Lancaster (1999, pp. 145). Measurements of these conditions within the tunnel, including the mass loss per unit area as well as the mass transport rate, were obtained from DEM data captured with the Vivid scanner. In comparison, the fluid flow characteristics, specifically u_*, were calculated from vertical profiles of the streamwise velocity collected with the Dantec™ laser Doppler anemometer (LDA).

Shown in Figure 3-1 is a two-variable response surface illustrating in kg m^{-2} the net mass loss for the various wind speed (U_∞) and particle size distribution ($\%_C$) combinations, as measured at 50 minutes. Mass loss was calculated from the volume of sediment

removed, using ρ_{bulk} = 1500 kg m^{-3}, a commonly used value for quartz sands in aeolian studies (Lancaster, 1995). There is a clear relation apparent in Figure 3-1 between the wind speed and the mass loss (r = 0.434), although it is not statistically significant at α = 0.05, as r_{crit} = 0.468. Higher wind speeds create greater fluid drag on the bed surface and increase the transport capacity of the system (Bagnold, 1941). The positive correlation between net mass loss and U_∞ in this study is consistent with previous modelling and experimental results. However, this correlation analysis is complicated by the inclusion of five distinct bimodal particle size distributions. Most sediment transport studies have been conducted with either uniform or unimodal particle size distributions (e.g. Bagnold, 1941; Seppälä & Lindé, 1978).

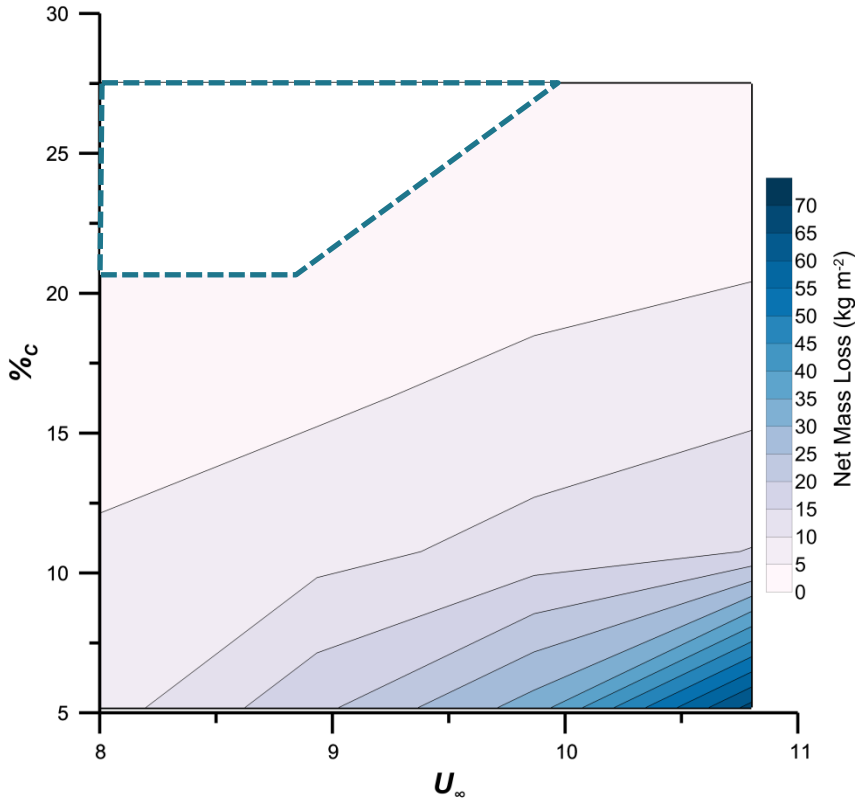

Figure 3-1 Net mass loss per unit area of bed surface at 50 minutes, demonstrating the interdependence of U_∞ and %C in influencing the amount of erosion. The hashed outline indicates an area where data were not collected.

Response surface analysis allows visualization in a two-variable space. Worthy of note is the inverse correlation between the proportion of the sample comprised of coarse mode particles ($\%_C$) and the net mass loss, which is statistically significant (r = -0.596; r_{crit} = 0.468). Increasing the proportion of the sample comprised of coarse mode particles ($\%_C$) decreases the sediment supply available for saltation at the beginning of the run (t = 0), as the larger coarse mode particles cover a larger proportion of the sand bed, thereby sheltering the fine particles. Throughout ripple development a larger $\%_C$ continues to contribute to a reduced availability of saltators, as winnowing further increases the proportion of the surface area that is comprised of coarse grains (β_C). As a result aeolian impact ripple systems are often classified as lag features (Greeley & Iverson, 1985). A quantitative analysis of the surface armouring process will be further discussed in § 3.6.

Rates of sediment transport were investigated using the time interval scans from the Vivid. To further reinforce the influence of the sample $\%_C$ on the sediment transport dynamics, Figure 3-2 shows the trend in the mass loss flux at U_∞ = 9 m s^{-1}, for samples 1 through 4. The general relationship appears to taper towards zero kg m^{-2} s^{-1} then displays random variation along the x-axis. Variations in the absolute value smaller than 0.001 kg m^{-2} s^{-1} lie within the range of the instruments precision, and are considered to be equal to zero.

Sample 4 initially exhibits mass gain, indicating an accumulation of particles within the sampling area. This is believed to be due to the creation of perched particles during the test bed preparation. Perched particles are significantly more susceptible to entrainment than a typical bed particle as they are highly exposed to drag, and thus are transported and deposited downstream during the initial exposure to the air flow. The surge in the downstream movement of the particles, when combined with the start/stop nature of the

interval scans, results in accumulation below the scanner within the measurement window. The influence of these perched particles is limited, and once they are removed from the bed, it is clear that transport ceases as in the case of Sample 4.

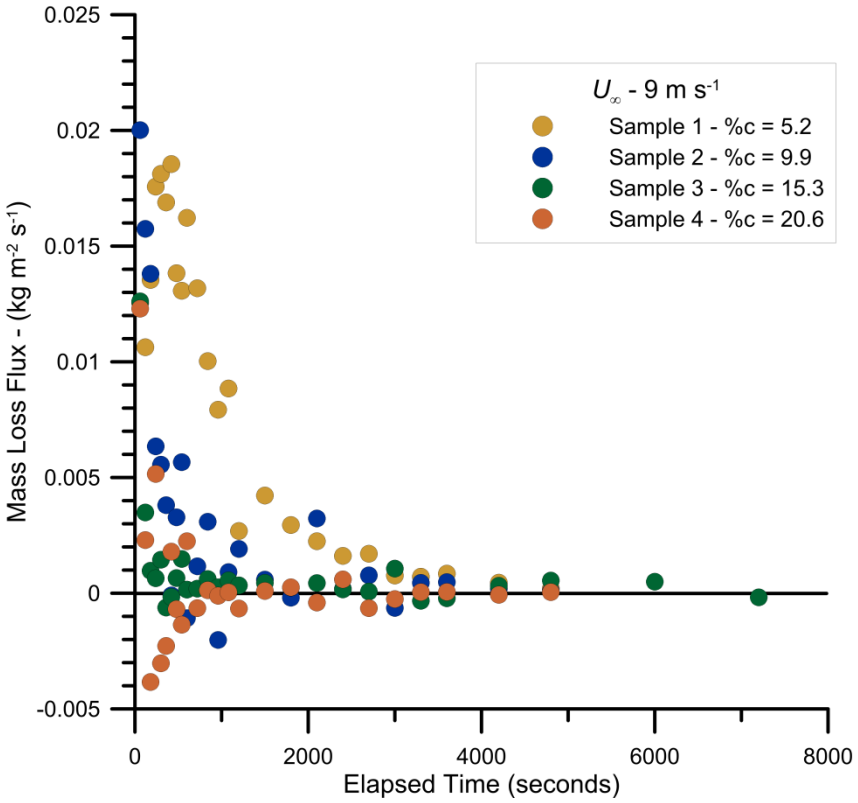

Figure 3-2 Mass loss flux at U_∞ = 9 m s^{-1} for Samples 1 through 4. Tapering to minor fluctuation around 0 kg m^{-2} s^{-1} is evident with time.

There is a statistically significant, positive correlation between the ripple amplitude and the net mass loss per unit area, as well as between the ripple wavelength and the net mass loss per unit area (*A:* r_A = 0.667; λ: r_λ = 0.797; r_{crit} = 0.468). This experimental evidence greatly reinforces the theoretical deduction that deflationary conditions are needed to form aeolian impact ripples, as discussed by Bagnold (1941) and Sharp (1963).

The time at which the system attains stability, with Q = 0 kg m^{-2} s^{-1}, is inversely proportional to the sample $\%_C$. The net rate of change in mass, Q, is equal to the difference between sediment lost and sediment supplied ($Q = Q_{out} - Q_{in}$). The inverse trend in Figure 3-2 indicates that the surface is undergoing an increased rate of armouring as the surface coarse mode proportion (β_C) increases, resulting in supply limited transport. Deflationary lag surfaces become supply limited through time, and it is clear that the higher the initial proportion of coarse mode particles, the sooner the system is starved of saltators.

Sediment transport models, e.g. the Bagnold Formula (Equation 3-1), often include the particle diameter and density as variables. In the case of a bimodal system with transport mode segregation, the mean particle diameter is an unsuitable measure when comparing different particle size distributions is unsuitable. Other measures have been explored, such as the coarsest twentieth percentile (P_{20}) (Ellwood, et al., 1975), or in the case of this thesis, the coarse mode percentage, $\%_C$. More importantly, relationships in this thesis that clearly depend upon both the wind speed and the sample $\%_C$ should be noted in future studies that attempt to refine transport models specific to bimodal systems.

$$Q = C\frac{\rho}{g}\sqrt{\frac{d}{D}}u_*^3 \qquad \text{Equation 3-1}$$

Q - Mass Transport Rate
C – drag coefficient
ρ – particle density
g – gravitational constant
d – particle diameter
D – reference diameter
u_* - friction velocity

3.2 Friction Velocity and Aerodynamic Roughness Measurements

Friction velocities for the wind tunnel runs were measured over a stable bedform, as described in the methods section of this thesis (§ 2.10, pp. 39). The values reported in Table 3-1 are intended to provide an indication of general fluid flow conditions within the tunnel.

The data in Table 3-1 were provided by Dr. Bailiang Li, who analyzed the velocity profile data to derive the values. A full analysis of the temporal variation of the frictional velocity and aerodynamic roughness length, as well as the fluid flow characteristics above the ripples, remains under investigation as a separate collaborative research project.

Table 3-1 Friction velocity (m s^{-1}) and aerodynamic roughness length (z_0) values

u_* / z_0	8 m s^{-1}	9 m s^{-1}	10 m s^{-1}	11 m s^{-1}
Sample 5 - %C = 27.5	-	-	0.40 / 0.02	0.50 / 0.06
Sample 4 - %C = 20.6	0.33 / 0.02	0.38 / 0.03	0.45 / 0.05	0.55 / 0.17
Sample 3 - %C = 15.3	0.33 / 0.02	0.42 / 0.06	0.50 / 0.12	0.59 / 0.25
Sample 2 - %C = 9.9	0.35 / 0.03	0.44 / 0.08	0.57 / 0.36	0.65 / 0.41
Sample 1 - %C = 5.2	0.41 / 0.08	0.50 / 0.22	0.59 / 0.39	0.55 / 0.20

3.3 Time Series of Topographic Expression

An aid for readers is shown in Figure 3-3, where optical data from the Vivid are draped over a Vivid DEM. The figure emphasizes the bedform by using three times vertical exaggeration, and should assist the reader in conceptualizing the correspondence of coarse (red) particles with ripple crests, and fine (beige) particles with ripple troughs.

To aid in visualizing the bedforms developed with the various wind speed and bed texture combinations, Figure 3-4 is a compilation of wind-aligned surface profiles, obtained over time, from the Vivid scans. The inception, evolution and stabilization of ripples are clearly evident in the figure.

The largest ripples were produced in combinations of high wind speed and a low proportion of coarse particles. The largest recorded amplitude was 10 mm, and the longest recorded wavelength was 140 mm. The high kinetic energy and abundant sediment supply allowed for rapid bedform development and high rates of erosion. While Sample 1 run at U_∞ = 11 m s^{-1} appears to be chaotic, the figure is affected by the high rate of surface deflation, which completely eroded the sand bed within 25 minutes.

Little to no bedform development occurred at low wind speed given a high proportion of coarse particles. Any minor development was likely a relic of the bed preparation method, which produced a thin layer of perched particles. The short duration of transport for these perched particles produced minor topographic variation on the bed surface. Such topographic variations should be considered aeolian *proto-ripples*, and certainly not fully developed aeolian impact ripple forms. Their small amplitude, lack of distinct wavelength, and timeframe of development discount them from being considered the same as the other impact ripples formed under more energetic conditions.

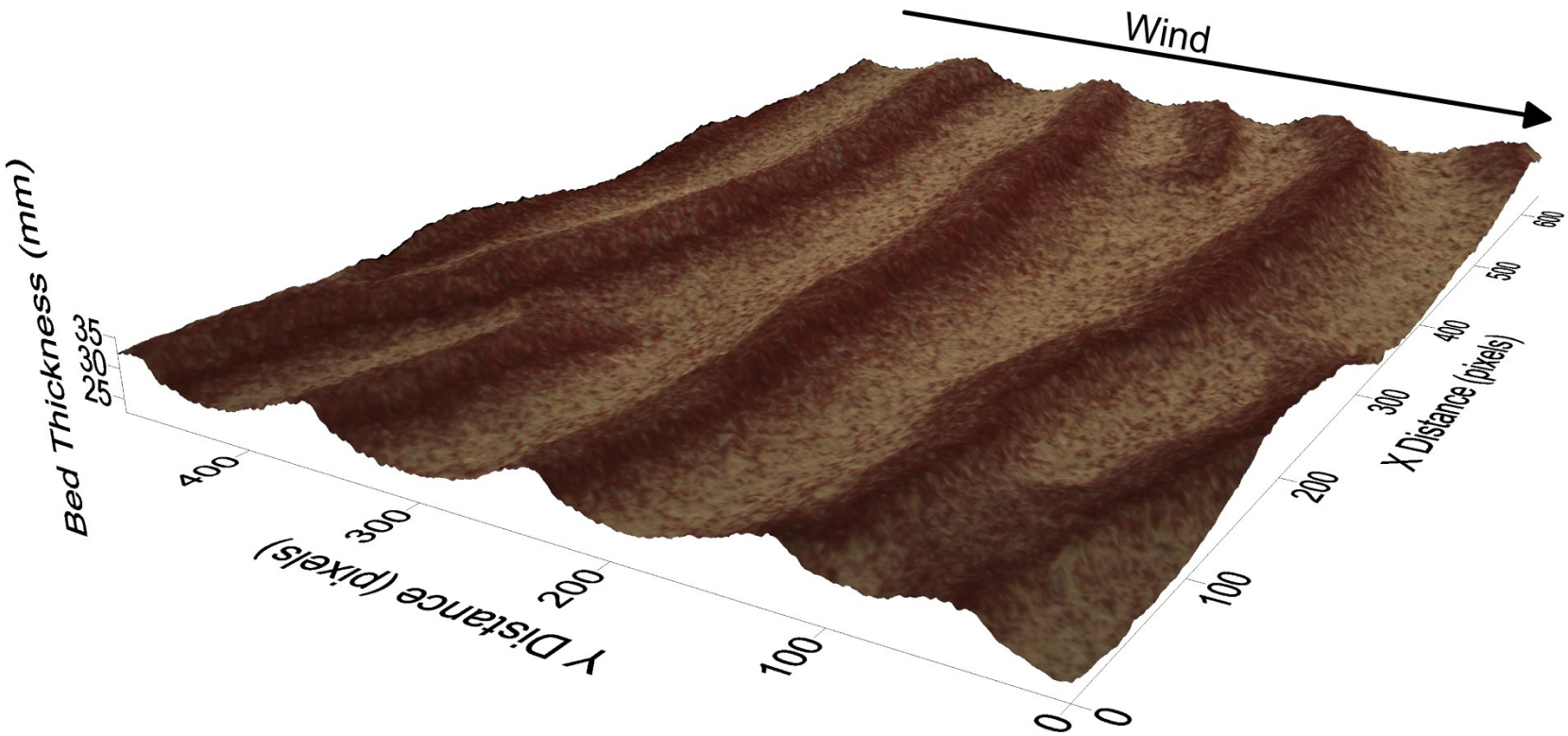

Figure 3-3 Three dimensional digital elevation model of ripple topography for Sample 1 after 50 minutes of exposure to 9 m s^{-1} wind. Optical data from the Vivid are draped over DEM data from the Vivid. Three times vertical exaggeration emphasizes the ripples, as well as the placement of coarse (red) particles in relation to the fine (beige) particles.

SAMPLE 1 $\%_C$ = 5.2

8 m s^{-1}

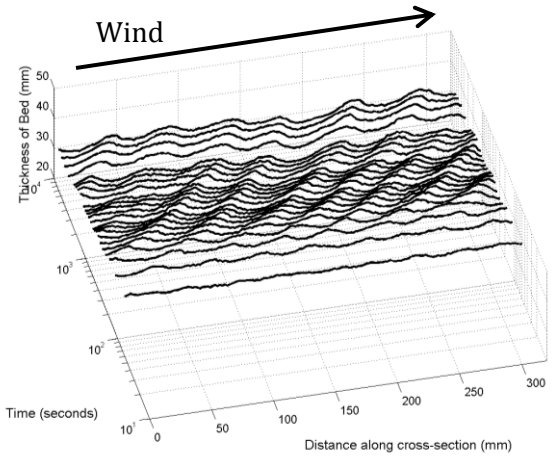

9 m s^{-1}

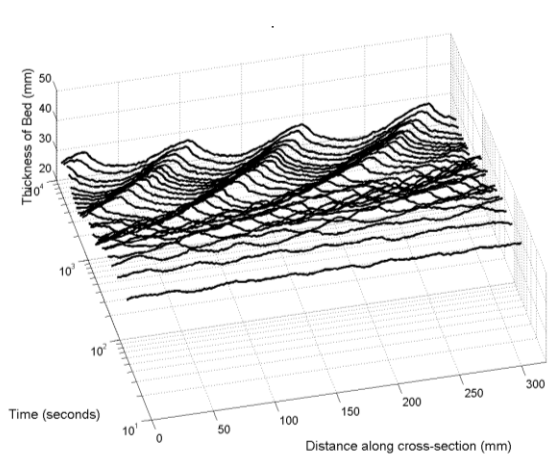

10 m s^{-1}

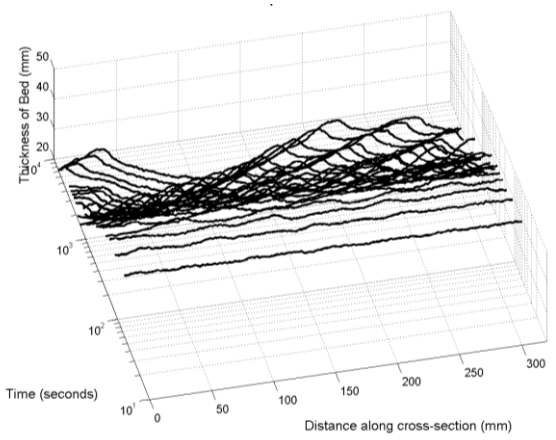

11 m s^{-1}

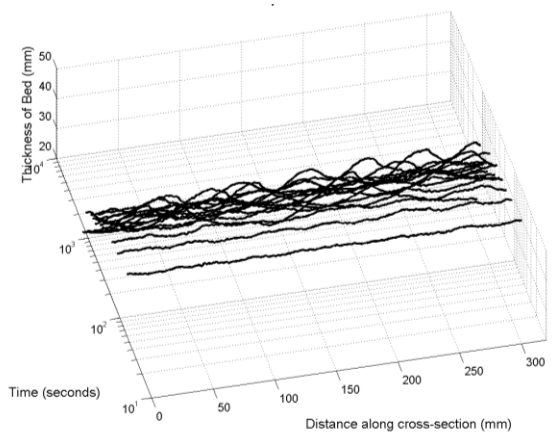

SAMPLE 2 $\%_C$ = 9.9

8 m s^{-1}

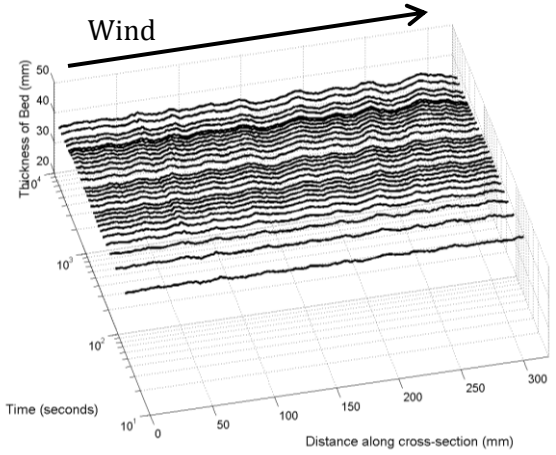

9 m s^{-1}

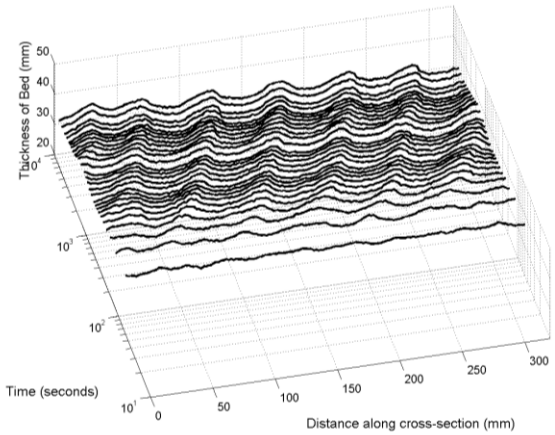

10 m s^{-1}

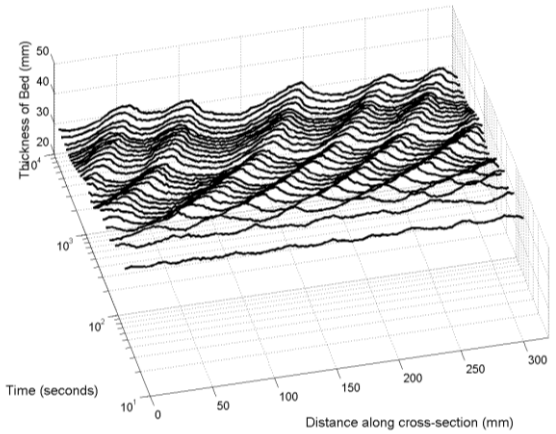

11 m s^{-1}

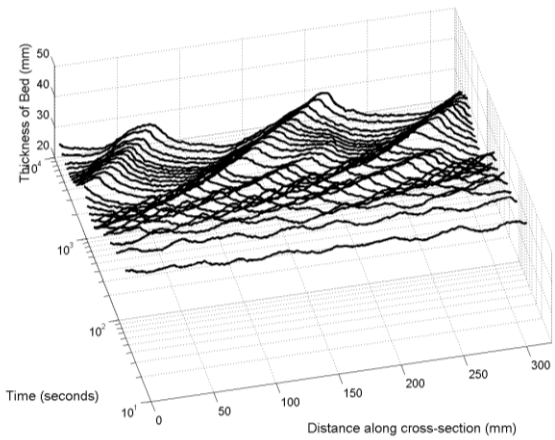

SAMPLE 3 $\%_C$ = 15.3

8 m s^{-1}

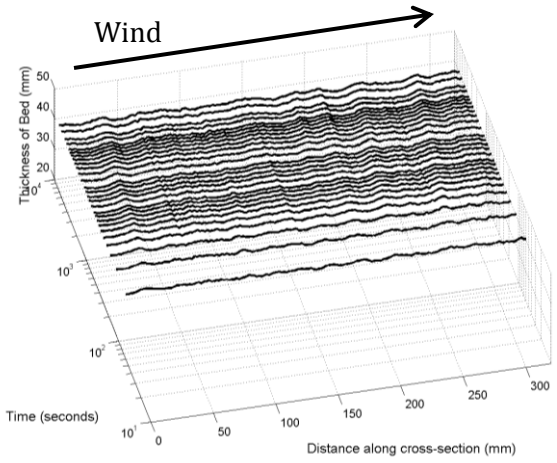

9 m s^{-1}

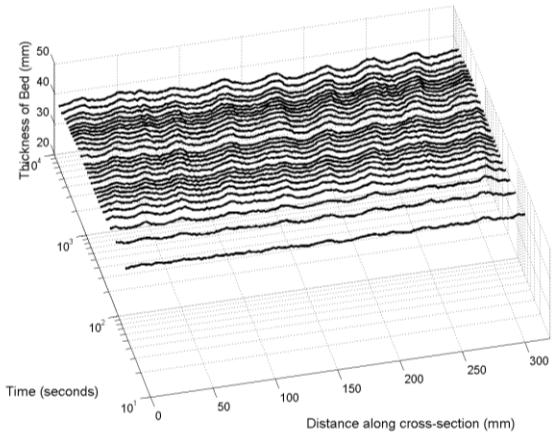

10 m s^{-1}

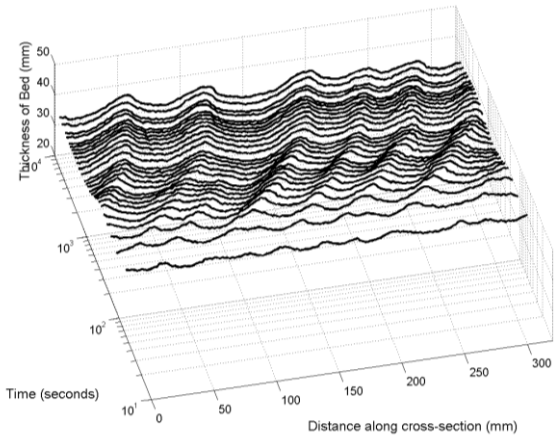

11 m s^{-1}

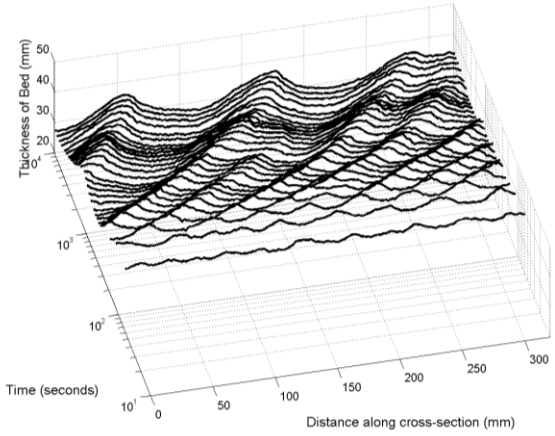

SAMPLE 4 $\%_C$ = 20.6

8 m s^{-1}

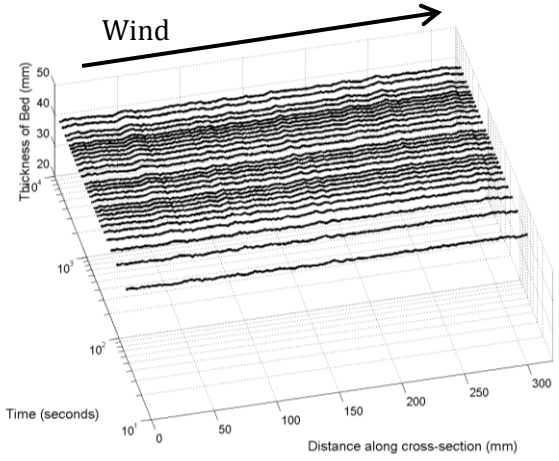

9 m s^{-1}

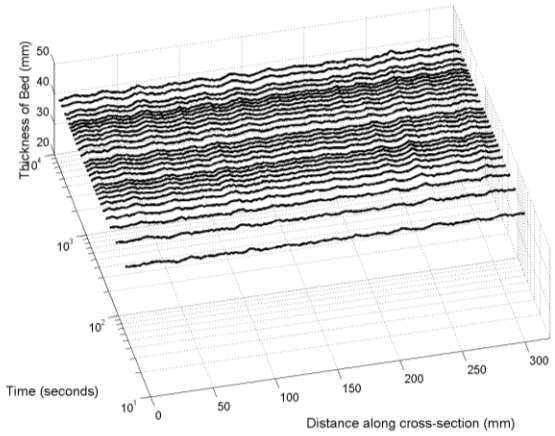

10 m s^{-1}

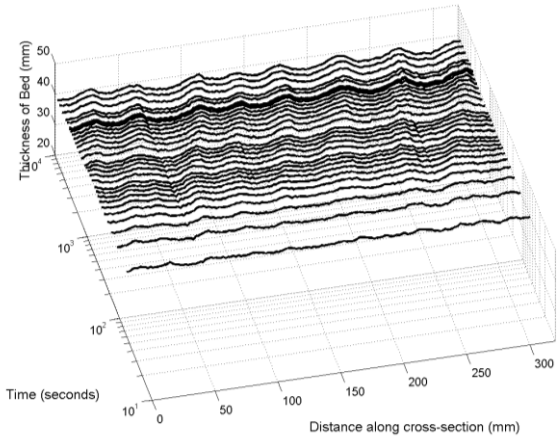

11 m s^{-1}

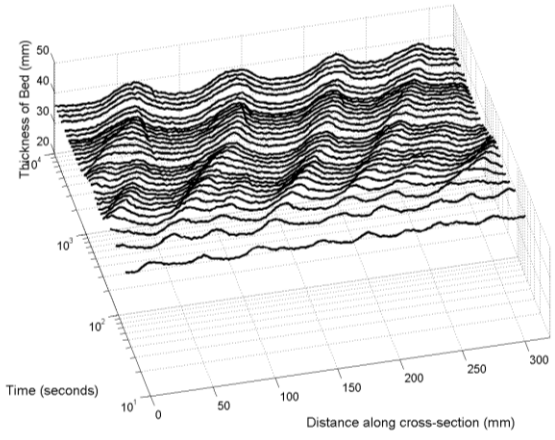

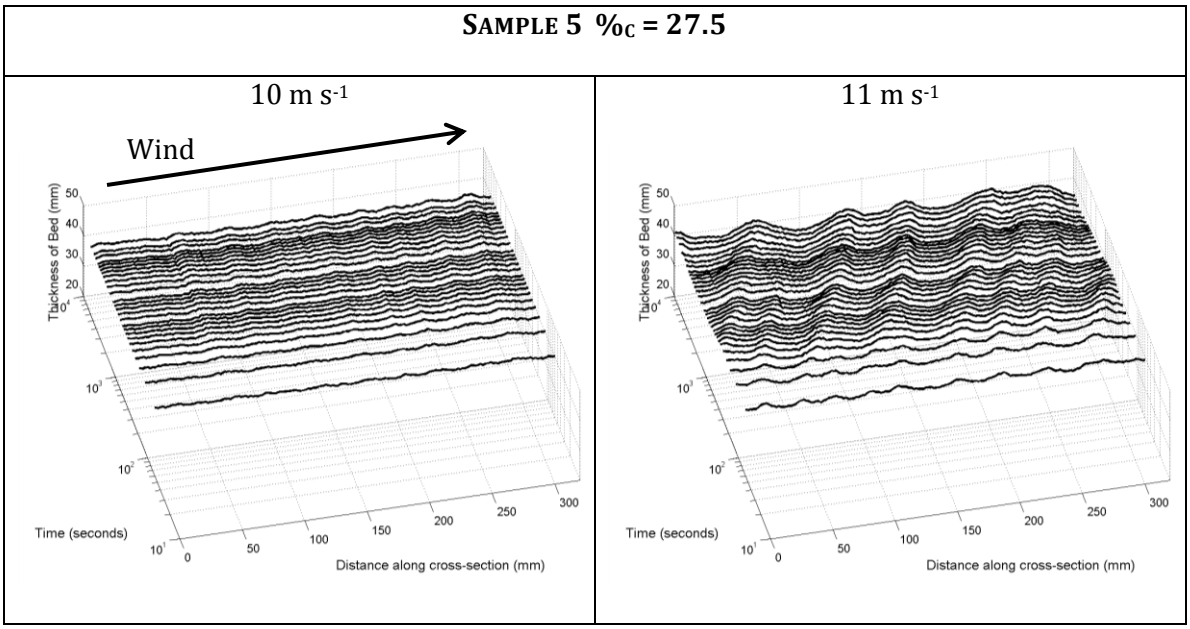

Figure 3-4 Wind direction from left to right. Compiled cross sections from Vivid scanner data. Cross-sections with 2mm grid node separation were taken from the centre of each surface. The x axis represents the distance along the streamwise cross section and the z axis represents the thickness of the sand bed. Of important note is the logarithmic scale of the y axis, which represents time. Scan intervals can be found in Table 2-4.

3.4 Ripple Morphometrics – Amplitude, Wavelength, Ripple Index, and Ripple Symmetry Index

The cross sectional data compiled in Figure 3-4 served as a basis for measurement of various ripple morphometrics. Ripple amplitudes ranged between sub-millimetre up to ten millimetres while ripple wavelengths ranged between 20 mm and 140 mm. Ripples tended to increase in amplitude and wavelength with an increase in wind speed, as compared to a decrease with increasing proportion of coarse particles ($\%_C$) (Figure 3-5 A & B). The dependency of ripple amplitude and wavelength on $\%_C$ is less studied than that of windspeed, particularly considering that most studies are conducted with particle size distributions that are well sorted and strongly unimodal.

A)

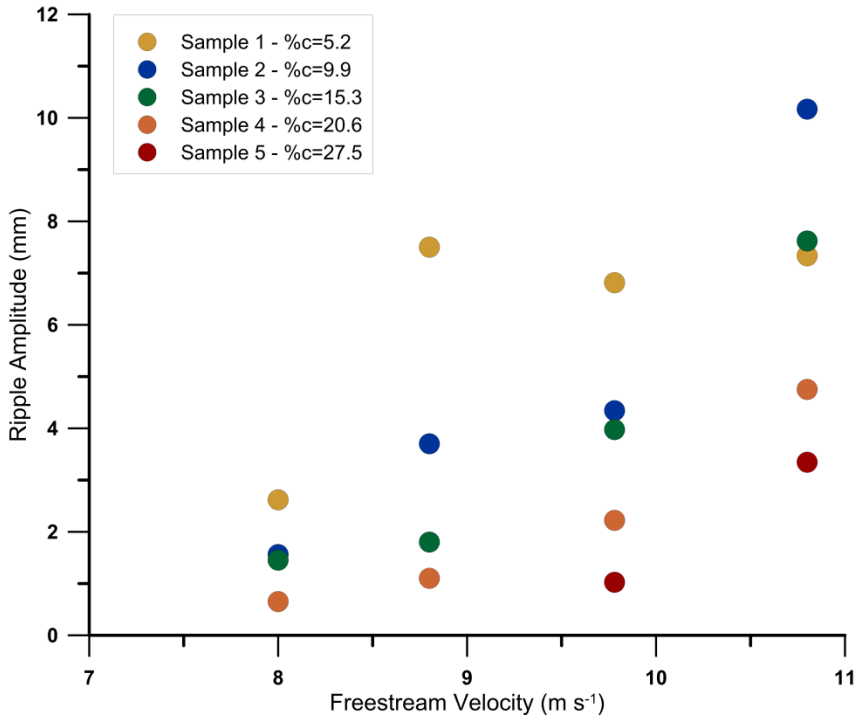

B)

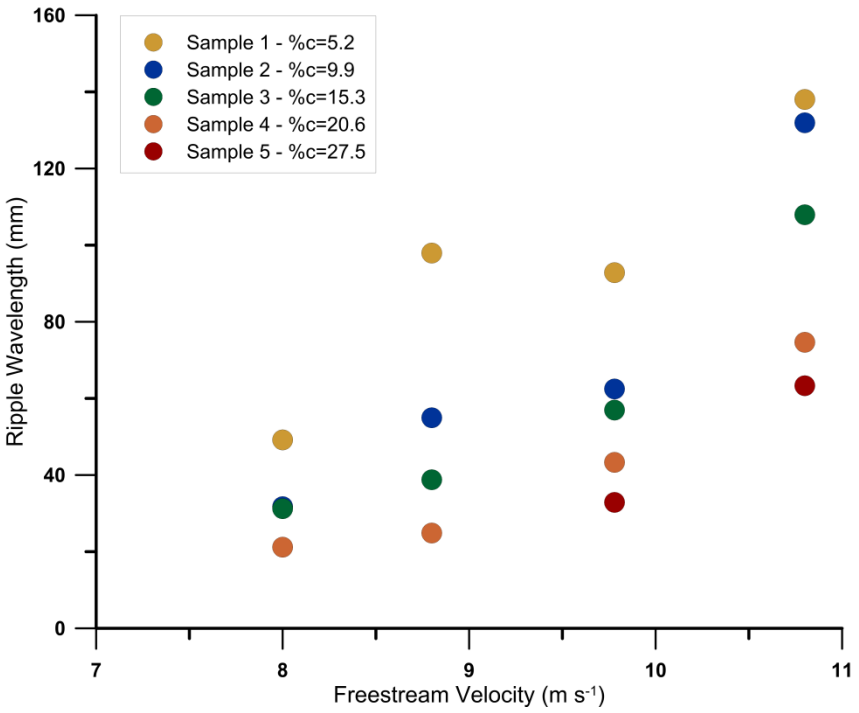

Figure 3-5 Effect of windspeed upon ripple A) amplitude and B) wavelength.

Aeolian megaripples are commonly reported to have a characteristic ripple index of 15, where $RI = \frac{\lambda}{A}$ (Yizhaq, 2008). In this regard, the ripples produced in this study are consistent with megaripples reported in the literature. Figure 3-6 shows that the deviation from the frequently reported value of RI = 15 is minimal, and it should be noted that published RI values for aeolian megaripples range between 10 (Cornish, 1914; as quoted in Pye & Tsoar, 1990) and 20 (Lancaster, 1995). A linear fit to the experimental data, forced through the origin, is shown in Equation 3-2.

$$\frac{\lambda}{A} = 14.86 \qquad r^2 = 0.97$$

Equation 3-2

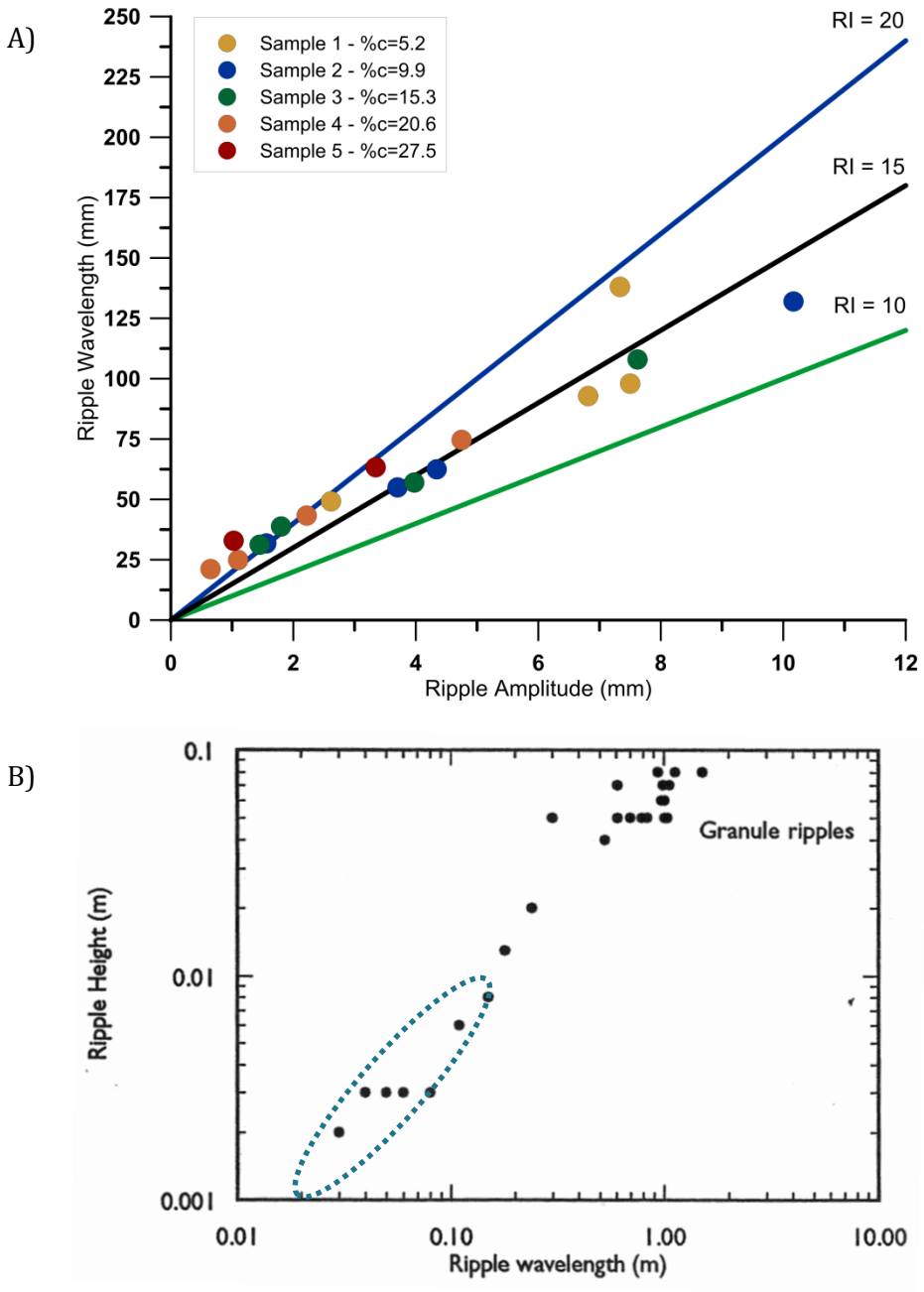

Figure 3-6 A) Ripple index showing clustering around the commonly reported value of RI =15. Included are RI = 10 and RI = 20 to illustrate the range of values reported in the literature for aeolian megaripples. B) Dashed oval indicates location of ripples created in this research within the published continuum of ripple heights and wavelengths (after Lancaster, 1995)

The strong correspondence between experimental data and the published values of ripple index illustrate that a system with similar transport dynamics to megaripples found in the field was created within the wind tunnel. This is important, as due to hardware

limitations, ripples could not be created that match the large scale of field ripples. Ripple index is an incomplete morphometric measurement, however, and should not be considered on its own without analysis of the components that it is derived from.

The ripples were generally symmetrical in shape (Table 3-2), as evaluated by the ripple symmetry index suggested in Pye & Tsoar (1990) (SI = stoss length/wavelength). While Lancaster (1999) reports that most wind ripples are asymmetrical, there is a range of indices and values reported in the literature for symmetry. Also, Lancaster (1999) reports that aeolian megaripples tend to be symmetrical as minor changes in the wind regime over the long time period of evolution can rework the surface, although this is not the case in a unidirectional wind tunnel. For the present study, the low U_∞, high $\%_C$ combinations fall significantly away from SI = 0.5, as seen in Table 3-2, further suggesting that they are relics of the bed preparation.

Table 3-2 Symmetry Index Measurements

	8 m s^{-1}	9 m s^{-1}	10 m s^{-1}	11 m s^{-1}
Sample 5 - $\%_C$ = 27.5			0.39	0.44
Sample 4 - $\%_C$ = 20.6	0.38	0.46	0.54	0.47
Sample 3 - $\%_C$ = 15.3	0.47	0.52	0.52	0.49
Sample 2 - $\%_C$ = 9.9	0.57	0.50	0.46	0.50
Sample 1 - $\%_C$ = 5.2	0.57	0.51	0.50	0.49

3.4.1 Morphometric Correlation with Freestream Velocity

Both ripple amplitude and wavelength are correlated to U_∞ (r_A = 0.63, r_λ = 0.70; r_{crit} = 0.47). This finding is consistent with current theoretical and experimental knowledge,

established for unimodal or uniform particle size distributions (Bagnold, 1941; Lancaster, 1995; Yizhaq, et al., 2004). Increased U_∞ values result in a higher transfer of energy to the sand bed particles, resulting in longer saltation and reptation path lengths (Anderson, 1987; Sharp, 1963). Whether considering either the characteristic saltation path (Bagnold, 1941) or reptation hop length (Sharp, 1963) as the driving force, the positive correlations between wind speed, ripple amplitude and ripple wavelength have been documented since the earliest works of Cornish (1914), and are noted in Bagnold (1941), Fryberger & Schenk (1981) as well as Seppälä & Lindé (1978).

Increased U_∞ values also increase the size of the largest particles that can saltate (Figure 1-5), which correspondingly increases the maximum size of particles that can undergo creep. The freestream velocities in this study were limited to those below the impact threshold for the smallest of the particles within the coarse (red) mode. With an increase in the freestream velocity, the additional energy transfer to the bed particles results in a greater proportion of the fine mode particles engaged in saltation. A saltating particle has the potential to move (via sliding or rolling) a particle up to six times its diameter (Bagnold, 1941), so that an increase in the maximum diameter of particles engaged in saltation results in an increase in the maximum diameter of particles undergoing creep. With a greater proportion of the particles found on a given surface engaged in transport (via saltation or creep), erosion and bedform development occurs more rapidly.

3.4.2 Morphometric Correlation with Particle Size Distribution

The ripples decrease in both amplitude and wavelength with increases in the proportion of coarse mode particles ($\%_C$). The negative correlations are statistically significant (r_A: -0.53, r_λ: -0.50, r_{crit}: -0.47). Increasing the $\%_C$ reduces the initial availability of

particles for saltation – the driving force behind the development of aeolian impact ripples. This is evident in Table 2-2 (Page 28) where increasing the $\%_C$ increases the fluid threshold for particle entrainment as measured using Wenglor sensors. As the number of collisions between the fine mode saltators and the coarse mode particles within the bed surface decreases, the rate of surface aggregation of the coarse particles due to creep correspondingly decreases, an important consideration as the coarse mode particles eventually form the crests of the ripples. As fewer particles are engaged in creep, there is a decrease in the overall rate of bedform development, and ultimately in the scale of the features that can be formed. This is evident in Figure 3-4, which illustrates the variations of ripple amplitude and ripple wavelength.

While surface armouring processes will be discussed in greater detail in 3.6, the influence of U_∞ and $\%_C$ on the ripple morphometrics can be effectively modelled with a multivariate approach as reviewed in the following section.

3.5 Multivariate Modelling of Ripple Amplitude and Wavelength

Visualizing the morphometric measurements in a two-variable response surface reinforces the patterns of influence of both U_∞ and $\%_C$, as shown in Figure 3-7. The upward diagonal trend is seen in both the amplitude (Figure 3-7 *A*), and the wavelength (Figure 3-7 *B*) plots. It should be very evident at this point that when discussing aeolian impact ripples it is impossible to focus attention solely on either wind speed or particle size distribution without telling an incomplete story. The multiple illustrations of this point within this thesis should hopefully guide the advancement of future CAM projects or numerical models of ripple development, such as those described in Yizhaq (2004) and Eastwood *et al*. (2011).

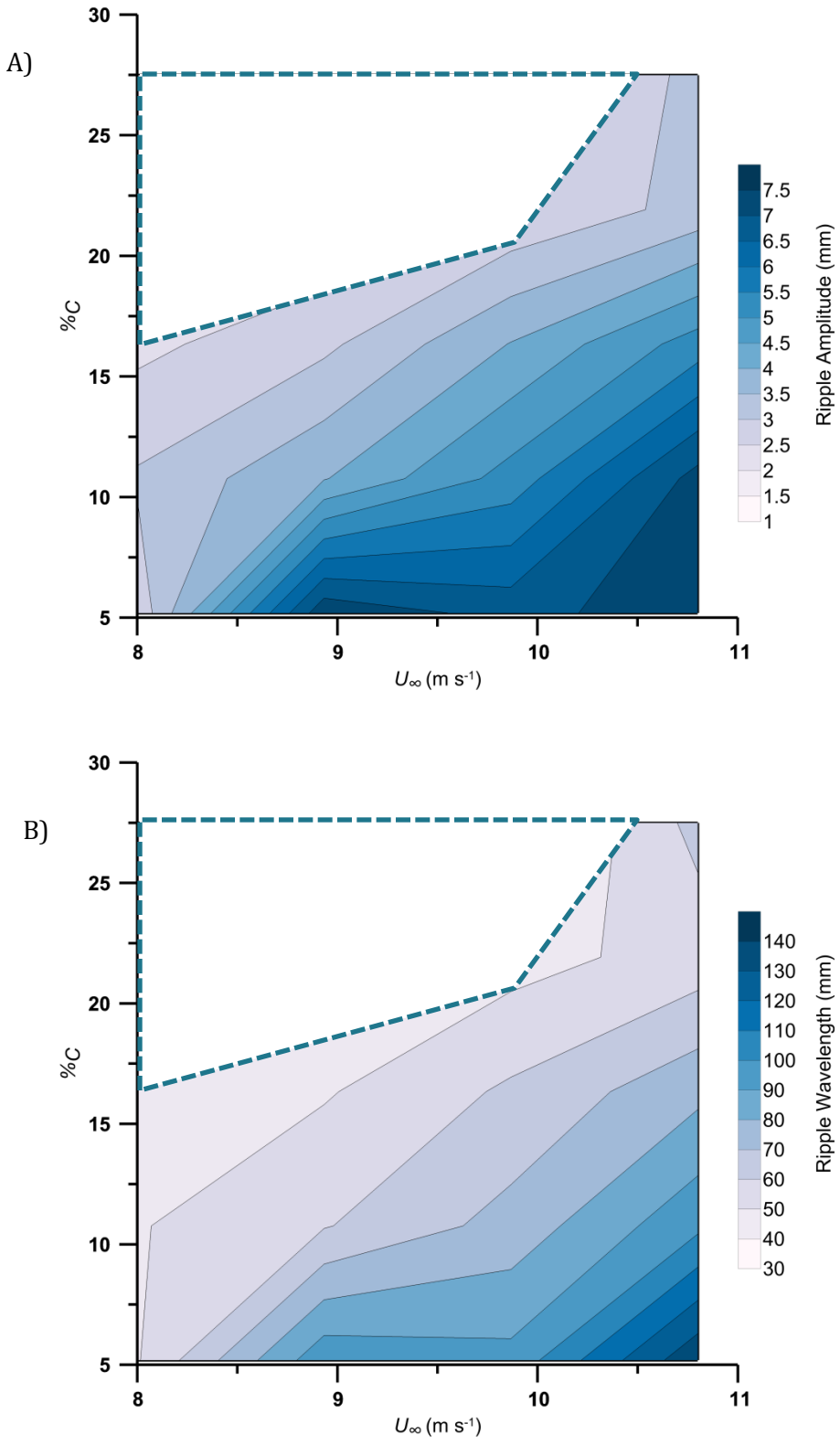

Figure 3-7 Two-variable response surface for A) Ripple Amplitude and B) Ripple Wavelength. Blacnk area overlays region of no data.

Considering the previous discussion linking the influence of both U_∞ and $\%_C$ on bedform development, it is only logical that a multivariate modelling approach takes into account both of these variables. The statistical models presented in Figure 3-8 are summarized below. These were created with experimental data from Sample 3 at 9 m/s, Sample 4 at 8 m/s and 9 m/s, as well as Sample 5 at 10 m/s removed. This was done as these combinations of $\%_C$ and U_∞ produced ripples inconsistent with the other bedforms.

$$A = 2.25\ U_\infty - 0.28\ \%_C - 13.37 \qquad \text{Equation 3-3}$$

$$r^2 = 0.78$$

$$\lambda = 31.56\ U_\infty - 3.72\ \%_C - 184.49 \qquad \text{Equation 3-4}$$

$$r^2 = 0.88$$

The predictive power of the statistical model for the ripple amplitude is shown in Figure 3-8 *A*. The model performs best in the case of lower to middle amplitude ripples, although there is more scatter in the larger amplitude ripples. Considering the range of values involved, and the homoscedasticity of the plot, it is clearly influenced by the higher concentration of data in the low amplitude, short wavelength range. When looking at the statistical model for predicting wavelength, Figure 3-8 *B*, the fit is tighter than that of amplitude, both visually and as indicated by the r^2 value (0.88). The statistical model once again provides the best fit for the shorter wavelength ripples where data is concentrated.

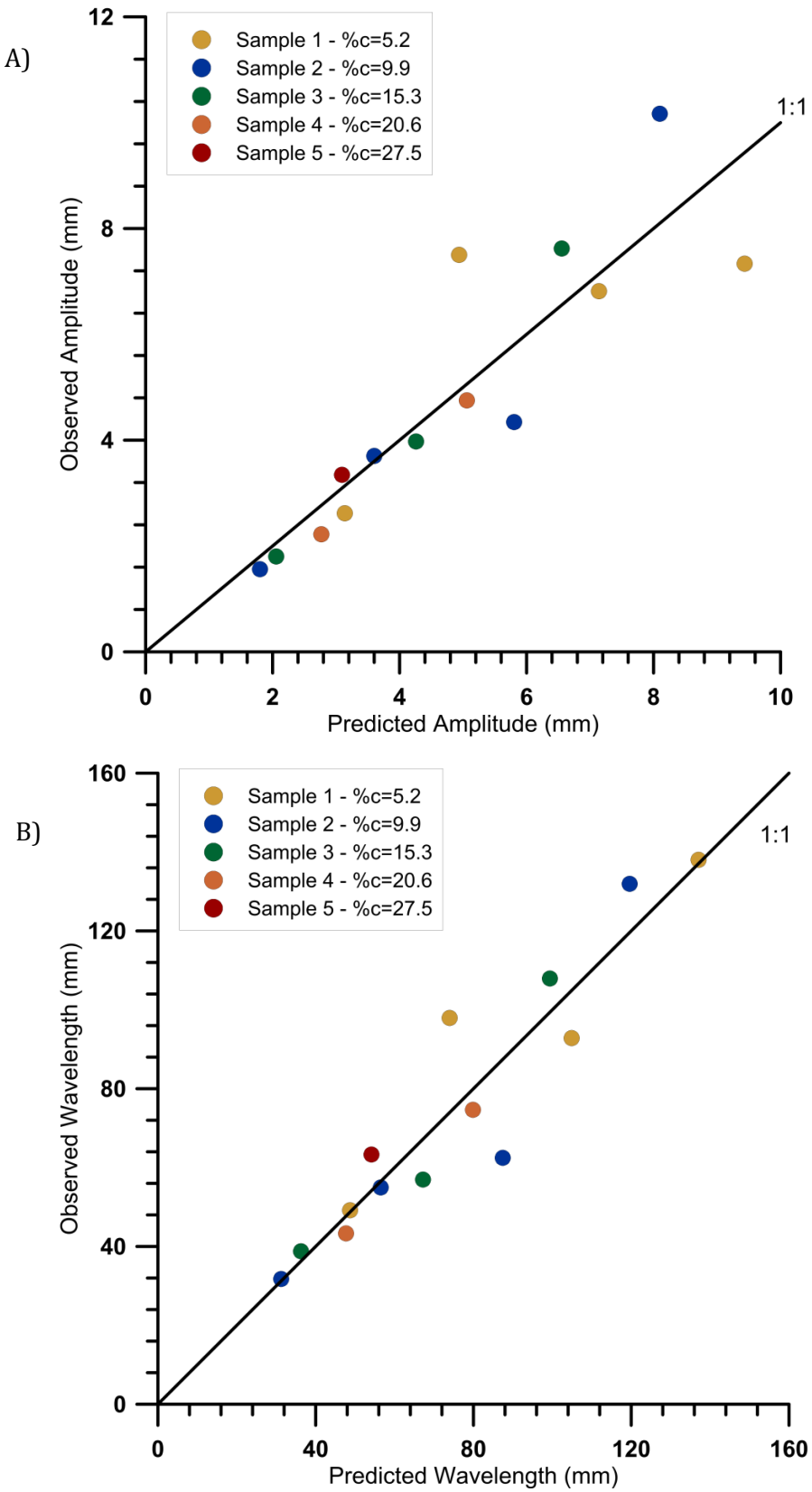

Figure 3-8 Multivariate statistical models predicting ripple A) amplitude, and B) wavelength.

Yizhaq (2004) states that it is not possible to account for the segregation of the two particle populations in the configuration of the numerical model he presents. An attempt is made by including parameter ε, which is an index of the mix of coarse and fine mode particles. A unimodal distribution is given $\varepsilon = 0$ (i.e. $\%_C = 0$), while an equal distribution of fine and coarse grains is given $\varepsilon = 1$ (i.e. $\%_C = 50$). The statistical models presented in Equation 3-3 and Equation 3-4, which incorporate $\%_C$, are easily related to the parameter ε, which should allow future models to be calibrated against experimental data.

Isenburg *et al*. (2011) speculate about the influence of particle size distribution on bedform development and morphology, stating that further experimental evidence is required (see Section 1.4.2, pp. 18). The relationships illustrated in Figure 3-8 help resolve this issue, as they demonstrate that for the system under consideration herein, increasing the $\%_C$ decreases both ripple amplitude and wavelength.

While the multivariate models illustrate that the system behaves in a predictable manner in terms of bedform morphometrics, the optical data reveal the grain scale interactions of this system, providing a qualitative and quantitative analysis of surface armouring and particle segregation. Such interactions are considered in the following section.

3.6 Surface Armouring Processes – Change in β_C

One of the most notable innovations of this study concerns the analysis of optical data to provide, at a grain scale, a measure of the influence of the wind speed and coarse mode proportion on particle segregation within a bedform. Historically the analysis of images captured for aeolian transport system has been conducted as a highly time

consuming manual process. This is exemplified by the work of Willets & Rice (1988) in which coloured grains of sand were visually counted on slide film in order to approximate mass transport by size fraction. Such techniques are limited in their capacity for both spatial and temporal resolution.

Optical data processing can quantify the proportion of the surface that is covered by coarse mode particles (β_C), which in this study are distinguished by their red colour. Additionally, statistics can be used to quantify the spatial organization of the two particle modes. An important distinction to make is that processing of optical data indicates the proportion of the surface area represented by the coarse mode particles (β_C), while the samples were created using proportion by mass ($\%_C$).

To aid in visualization of the bedforms in regard to particle mode segregation, Figure 3-9 incorporates composite images of each of the time series. The centre row of pixels from each image was extracted, and the rows were compiled into a single image. Time begins at the bottom of the image, with each pixel row separated by three seconds. It is clear that the segregation pattern of coarse mode particles (red) matches the bedform topography, which is especially evident when comparing Figure 3-9 with topographic cross sections in Figure 3-4. This is a highly visual representation, with grain scale detail, of the process described by Bagnold (1941), Sharp (1963), Anderson (1987) and Lancaster (1995), as reviewed in the introductory chapter of this thesis (§ 1.2, Page 2). The varying rates of accumulation and the migration of groupings of coarse mode particles as coherent units are also shown in Figure 3-9. Some of the very fine banding that occurs in the images is the result of surface particles remaining stationary, and is not the result of bedform development (i.e. Sample 4, 8 m s^{-1}). The composite images further validate that the

bedforms reached an equilibrium state, as the migration of the coarse mode particles ceases within the images, except in several isolated cases as previously discussed.

The increase in the proportion of the surface covered in red particles from the coarse mode, β_C, greatly influences the sediment transport system by limiting the supply of particles to the saltation cloud, changing the dynamics of collisions on the surface, as well as changing the characteristics of creep. As β_C increases, there is an obvious decrease in the supply of particles available for saltation as the proportion of the surface consisting of fine mode particles is equal to (1 - β_C). Furthermore, as the likelihood of a saltating particle impacting a larger particle within the coarse mode increases, the average saltation path length should increase (Manukyan & Prigozhin, 2009). As saltation paths increase in length, the flux of impacts correspondingly declines. Given that impacts from saltating particles are the driving force behind bedform development, these two points should not be overlooked. Finally, the higher the β_C, the more resistance a creeping particle will encounter. The transfer of momentum from the impact of saltating particles on the surface drives forward the coarse mode particles, which exhibit a lower rate of forward motion when they are surrounded by other coarse mode particles rather than by fine mode particles. This phenomenon was observed in images obtained where particles within the coarse mode migrated up the windward slope of a ripple and ceased motion. The windward slope is normally regarded as an area of preferential erosion, as it has a higher flux of impacting saltators than other areas of a given ripple (Bagnold, 1941). With the test beds examined, however, the coarse mode particles would cease motion when lodged among other coarse mode particles within the ripple stoss and crest.

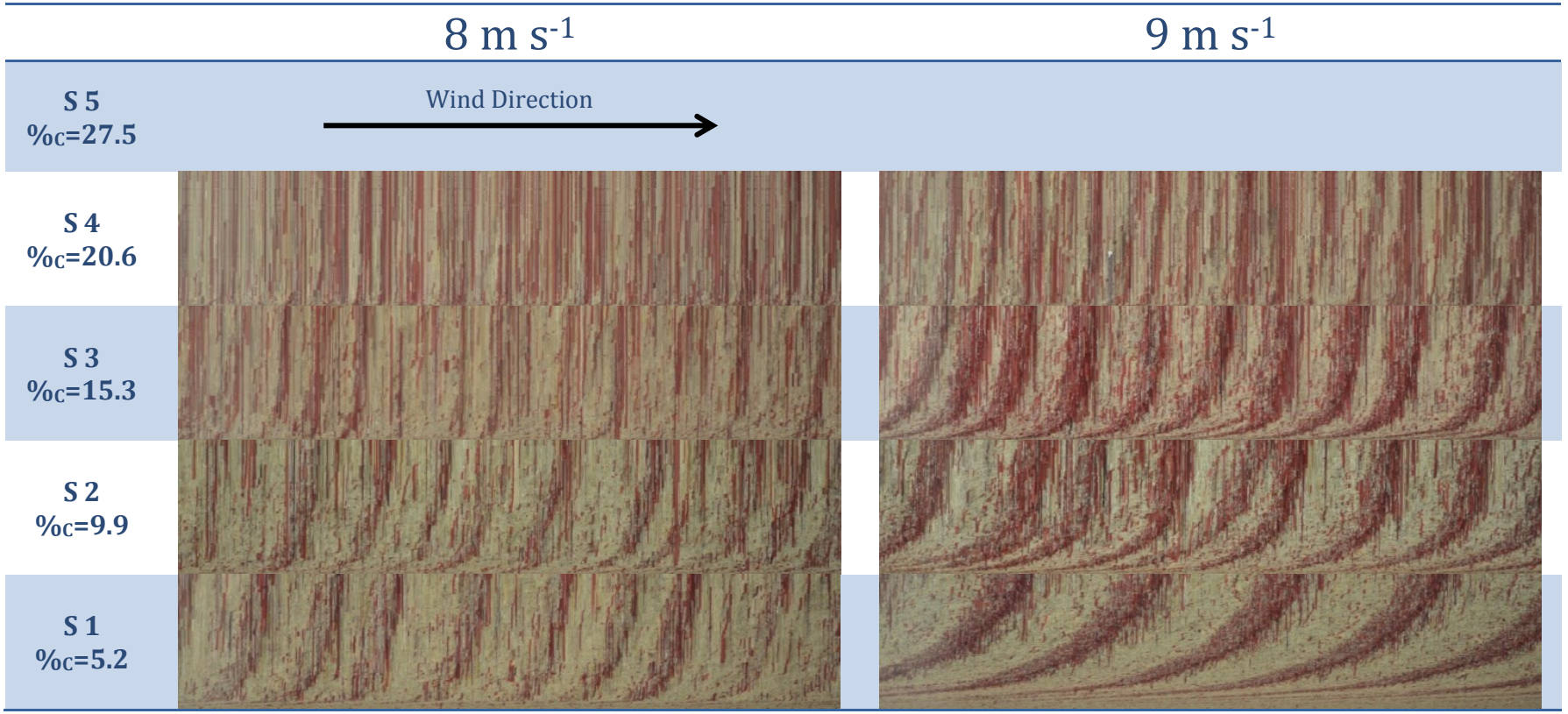
8 m s-1
9 m s-1
S 5
%c=27.5
Wind Direction
S 4
%c=20.6
S 3
%c=15.3
S 2
%c=9.9
S 1
%c=5.2

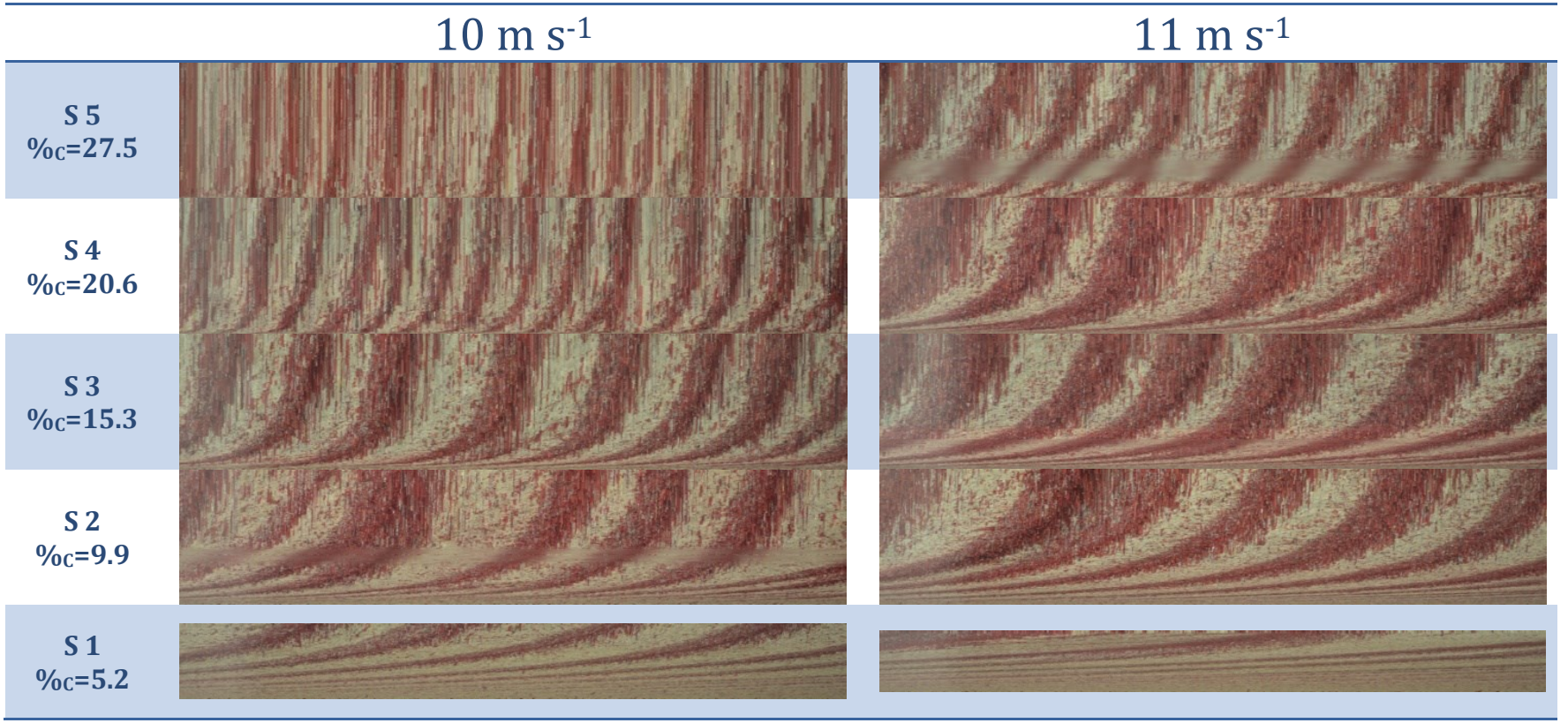

Figure 3-9 Composite images created by the extraction of the centre row of pixels for each image in the time series. Time increases from bottom to top, with wind blowing from the left to right in the images.

The change in β_C was measured by dividing the measurement obtained at the end of the optical run by the average starting value, providing the coarsening factor (CF). A two-variable response surface of the coarsening factor is shown in Figure 3-10 ***A***. Indexing was carried out to illustrate the change in the surface proportion, rather than just highlight the final proportion, as it should be clear that Sample 5 would naturally have the highest starting β_C, as it has more than five times the content of coarse mode by mass than Sample 1 ($\%_{C1}$ = 5.19, $\%_{C5}$ = 27.49). A multivariate statistical approach to modelling the temporal change is shown in Figure 3-10 ***B***, with the model equation shown below.

$$CF = 0.65U_{\infty} - 0.17\ \%_C - 1.86 \qquad \text{Equation 3-5}$$
$$r^2 = 0.77$$

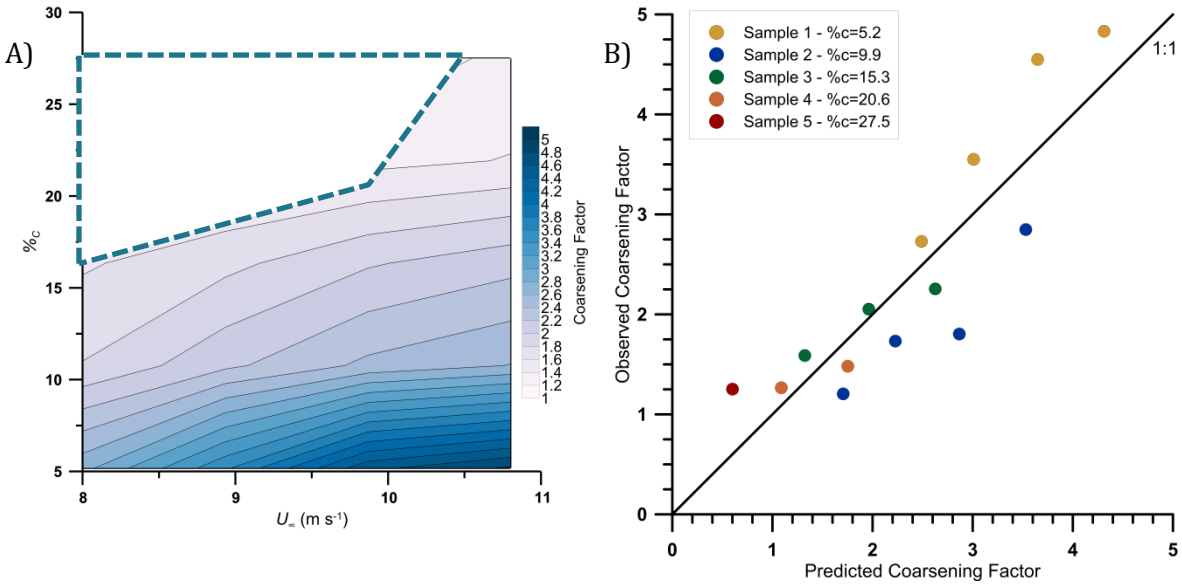

Figure 3-10 A) Response surface for the surface coarsening factor. B) Comparison of multivariate statistical model predictions to observed values for the coarsening factor.

The coarsening factor analysis illustrates that the equilibrium bedform surface is up to five times as coarse as the parent source, as measured by β_C. Sharp (1963) states that at least a 50% surface coverage of coarse mode particles is needed for ripple formation,,

although this value is attributed specifically to the crest region. Yizhaq (2004) found through numerical modelling that a minimum proportion of coarse mode particles are necessary for the development of ripples, although he does not explicitly state a value. He explored coarse mode to fine mode diameter ratios of 3-7, a range slightly larger than that of this research (d_c/d_f = 2.4). While the lower limit of $\%_C$ for the development of ripples was not investigated for this thesis, the upper limit was reached for three of the four wind speeds studied, as shown in both Figure 3-4 and Figure 3-9 where low U_∞, high $\%_C$ combinations failed to yield a bedform. This indicates that a range of wind speed and particle size distribution exists over which sediment transport dynamics are optimized for aeolian impact ripple formation.

3.6.1 Localized Surface Armouring

The surface armouring process was further investigated with the localized β_C metric, as shown in Figure 3-11. Streamwise strips from the centres of the optical images were divided into 75 subsets, 0.5 cm x 0.5 cm (0.25 cm^2) in size, and analyzed. Rows in Figure 3-11 are temporally separated by three seconds, which is the imaging interval. Local values of β_C = 0 and β_C = 1 are only obtained for processed images that are out of focus.

The coalescence of ripples and the development of clear groupings of the coarse mode and fine mode particles is shown in the figure. Referring back to Figure 3-3, patterns of high values of β_C match the locations of ripple crests and low values of β_C match the locations of ripple troughs. This figure supports, in very high spatial and temporal resolution, the work of Sharp (1963) in which he claimed that coarse mode particles make up 50-80% of the ripple crest but only 10-20% of the ripple trough. The results in Figure

3-11 suggest that this difference may actually be even larger than previously reported with particle mode segregation approaching 100% on the ripple crests. Furthermore, the ripple troughs in this study exhibit β_C values as low as the parent particle source. Localized values of β_C in the trough approach that of $\%_C$, although β_C is determined optically and $\%_C$ is determined by mass. Worthy of note are the remarkably sharp boundaries between regions having a high concentration of coarse mode particles and those of low concentration. In the case of $\%_C/U_\infty$ combinations that only developed proto-ripples, it is apparent that no developed pattern of spatial segregation occurs. The fine banding is the result of surface particles remaining stationary after being influenced by the saltation of perched grains, as was shown in Figure 3-9. This analysis provides the highest spatio-temporal resolution data obtained to this date that support the works of Bagnold (1941), Sharp (1963), Anderson (1987), and Isenburg *et al*. (2011).

SAMPLE 1 $\%_C$ = 5.2

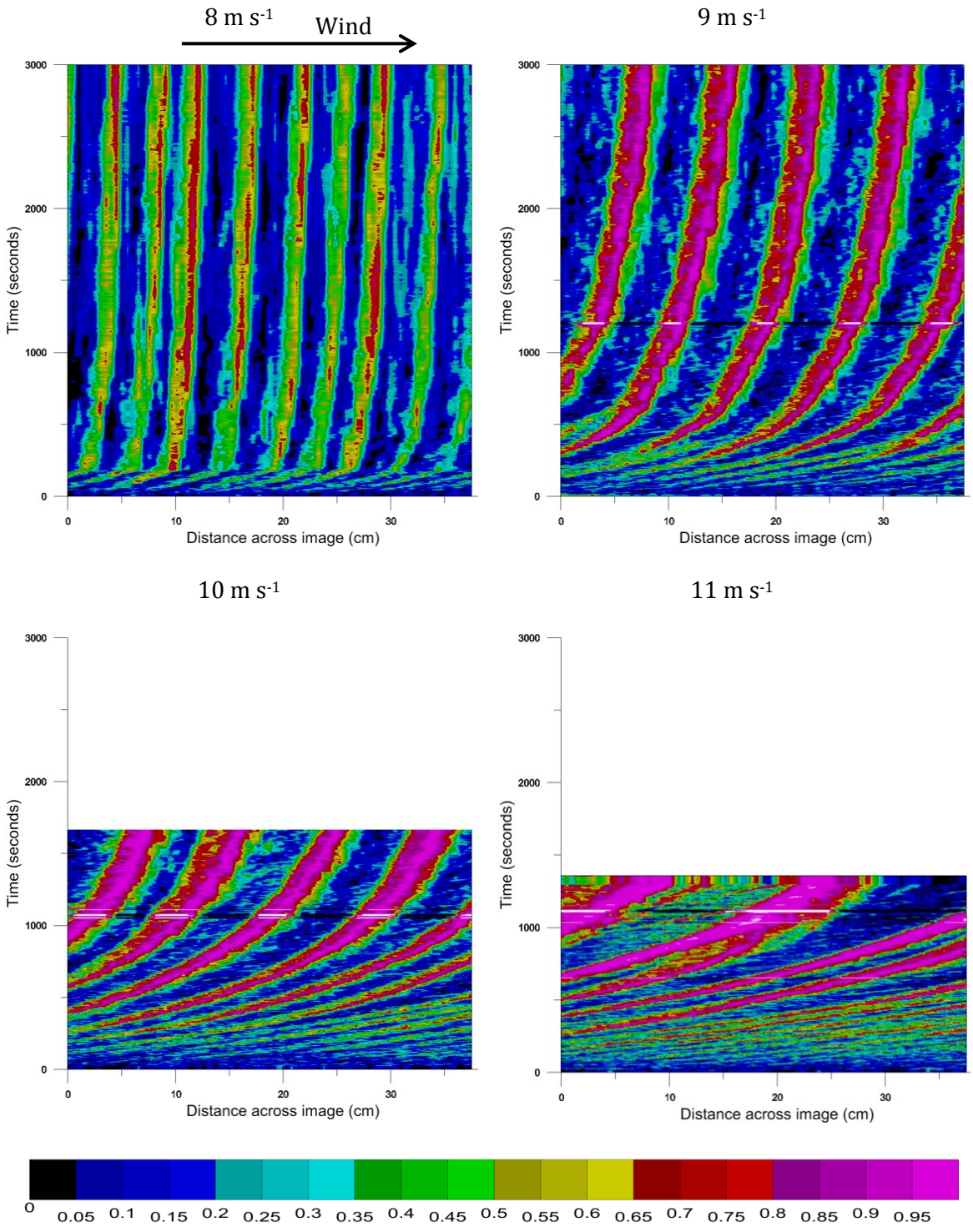

Local β_C metric calculated from 0.25 cm^2 subsamples

SAMPLE 2 $\%_C$ = 9.9

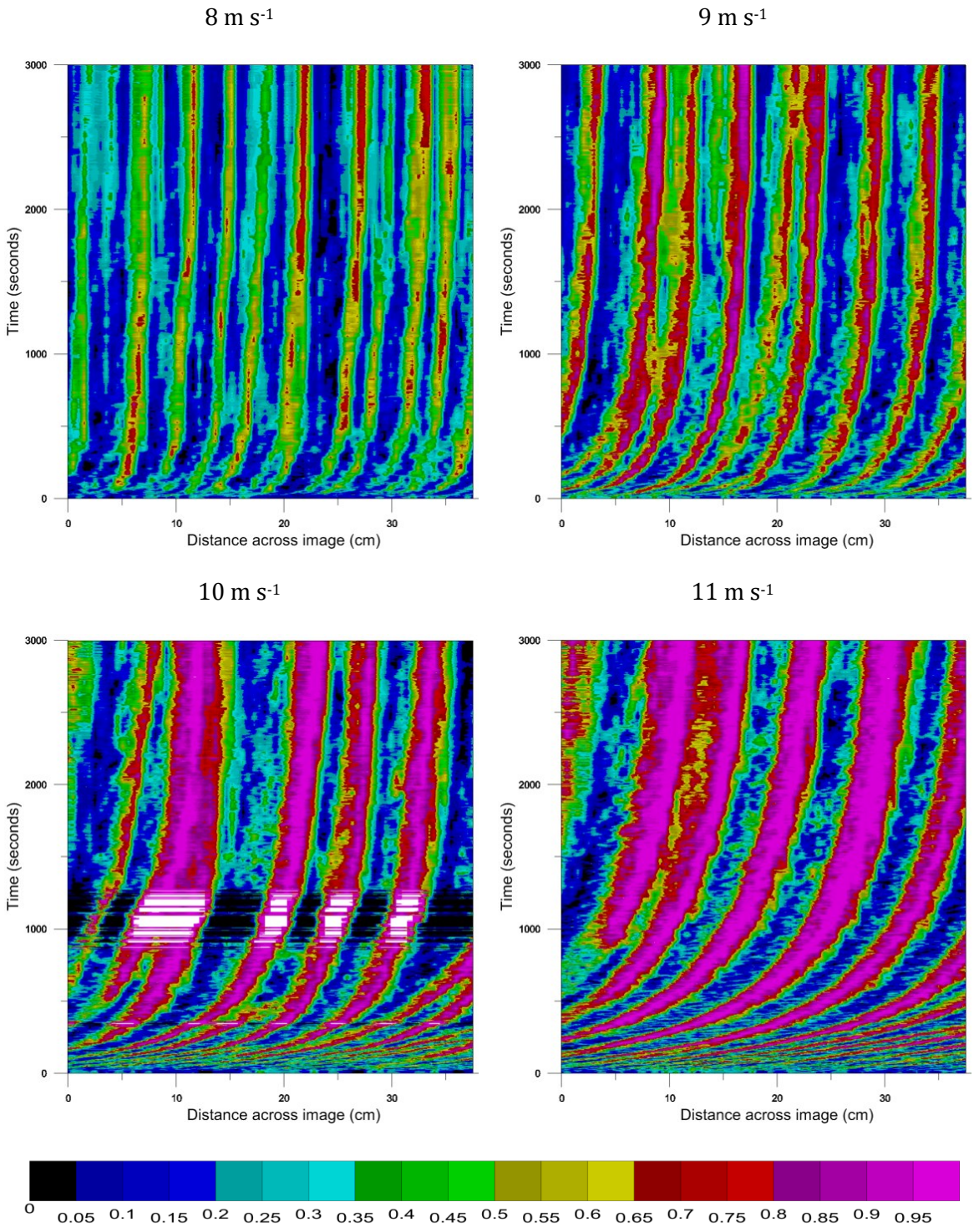

Local β_C metric calculated from 0.25 cm^2 subsamples

SAMPLE 3 $\%_C$ = 15.3

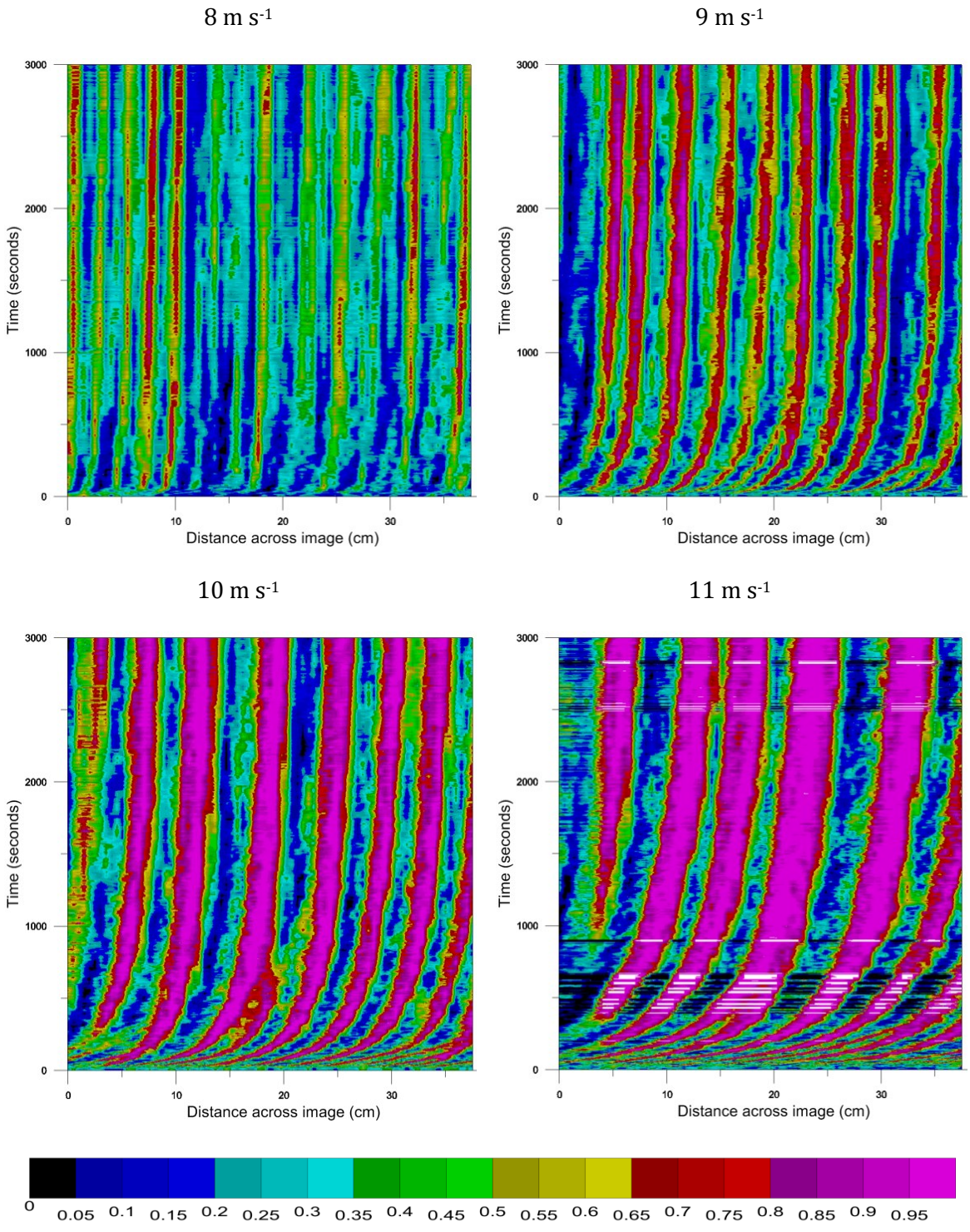

Local β_C metric calculated from 0.25 cm^2 subsamples

SAMPLE 4 $\%_C$ = 20.6

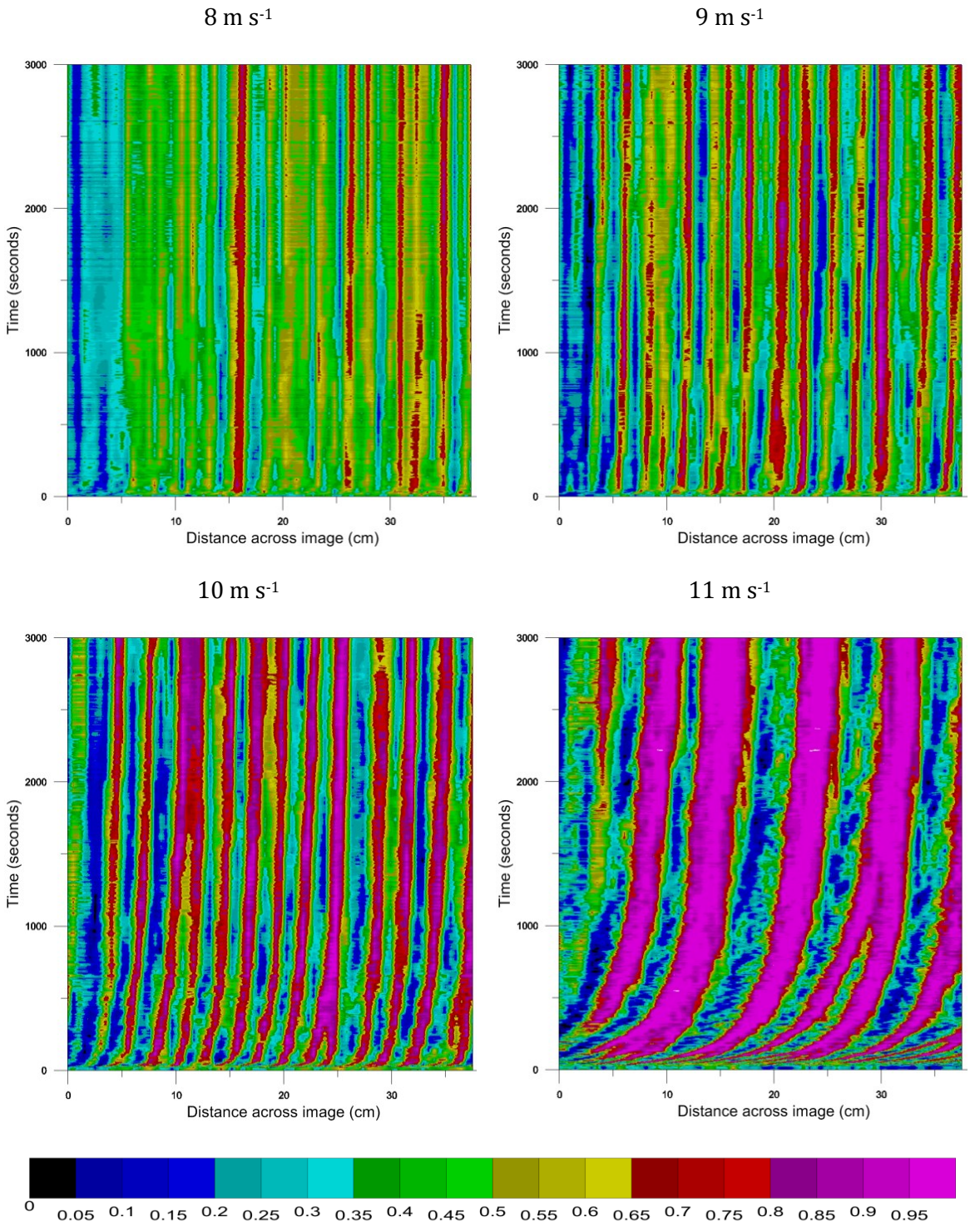

Local β_C metric calculated from 0.25 cm² subsamples

SAMPLE 5 $\%_C$ = 27.5

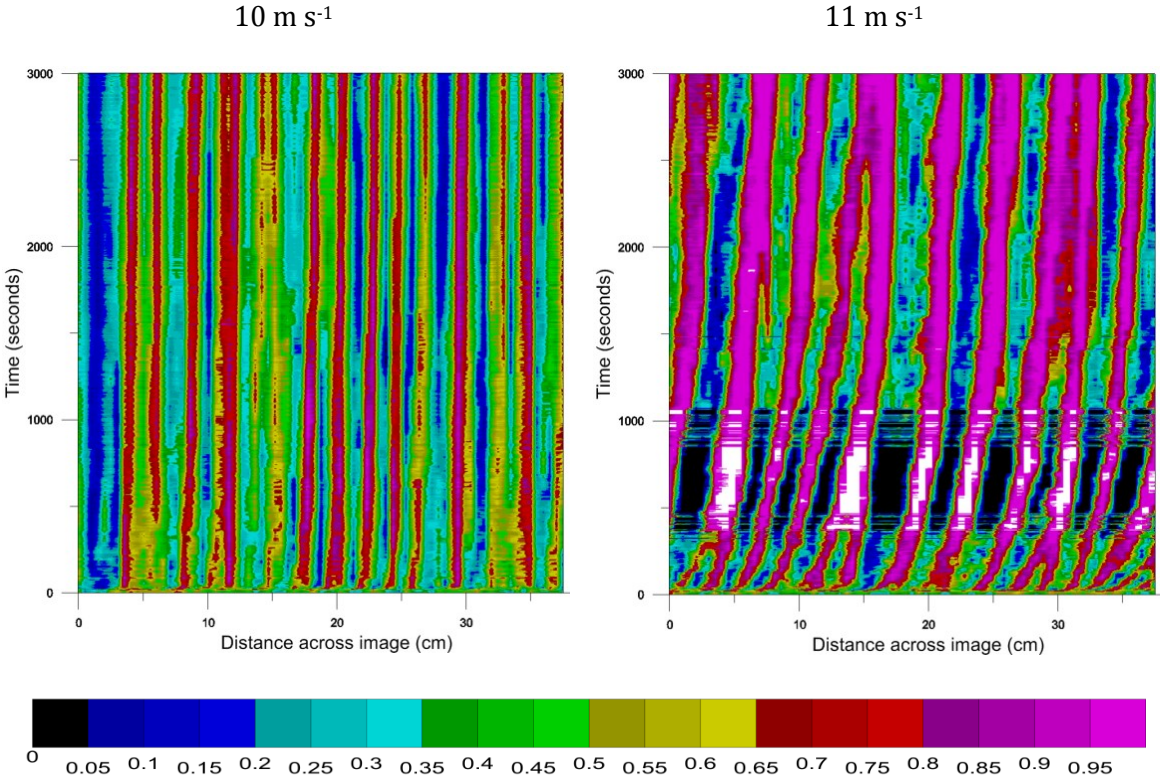

Local β_C metric calculated from 0.25 cm^2 subsamples

Figure 3-11 Localized surface coarseness (β_C) map created from 0.25 cm^2 subsets of optical images. 75 subsets in the streamwise direction were extracted from each optical image. Pixel rows are temporally separated by 3 seconds. In the case of blurry images, it is seen that β_C may reach the limits of 0 or 1.

3.7 Indices of Spatial Segregation

While the calculation of β_C as a global or local metric provides information about surface armouring, it was originally hypothesized that by taking advantage of the nature of digital images, spatial statistics could quantify the segregation of the two particle size modes. Quantifying the degree of spatial organization is a central issue in spatial analysis (Shortridge, 2007). Moran's I statistic, I, is an index that quantifies the degree of spatial relatedness of neighbouring elements (Fortin & Dale, 2005), and is commonly used in spatial analysis (Dale & Fortin, 2002). Moran's I was extensively explored for this dataset; however, it was not informative as a spatial statistic. A detailed analysis of the limitations of using Moran's I statistic with this very large dataset is available in the Appendix.

Perimeter to surface area ratios are commonly used in human geography, and are particularly well suited to census-style data analysis (Lee & Culhane, 1998). By applying perimeter to surface area ratio (PSAR) analysis to the digital images of this thesis, it is possible to quantify the spatial segregation between the two modes of particles. A decreased PSAR indicates that for a given surface proportion of coarse particles (β_C), the boundary length between the coarse mode particles and fine mode particles is minimized. This indicates that the two particle populations are more spatially segregated. As an example, a circle has the lowest PSAR for a 2-D geometric shape.

When using digital images, a surrogate for the perimeter of the boundary between two pixel values is the count of pixels that are considered an edge. Matlab Mathworks Image Processing Toolbox contains the function *edge()*, which provides a count of pixels in an image that have an adjacent pixel that differs in value. Applied to the optical images of the sand beds, if a pixel representing a coarse mode particle is adjacent to a pixel

representing a fine mode particle, then the pixel is labelled as being an edge. The proportion of the image that is considered an edge (β_E) was used in place of perimeter. A clustering index was calculated by dividing the proportion of the image that is classified as an edge (β_E) by the proportion of the image that is classified as a coarse mode particle (β_C), i.e. $C_I = \frac{\beta_E}{\beta_C}$. The results of cluster index analysis for the various combinations of U_∞ and $\%_C$ are presented in Figure 3-12 as a two-variable response surface and as a multivariate statistical model in Equation 3-6.

$$C_I = -0.052\, U_\infty + 0.0003\, \%_C + 0.68 \qquad r^2 = 0.85$$ Equation 3-6

There is a strong negative correlation between the C_I and U_∞ (r = -0.92) that is apparent in the pattern in Figure 3-12 **A**. In comparison, the correlation between C_I and $\%_C$ is not statistically significant (r = -0.38). This result most likely arises from the strong correlation of β_C to U_∞, illustrating that even with changing proportions of coarse mode particles, wind speed is most influential with regards to spatial segregation. As wind is the source of energy for an aeolian impact ripple system, the correlation of wind speed with this index should appear intuitive. It is still important to note that while the wind speed is the greater influence, the particle size distribution characteristics do play a role, and the two cannot be considered entirely separate.

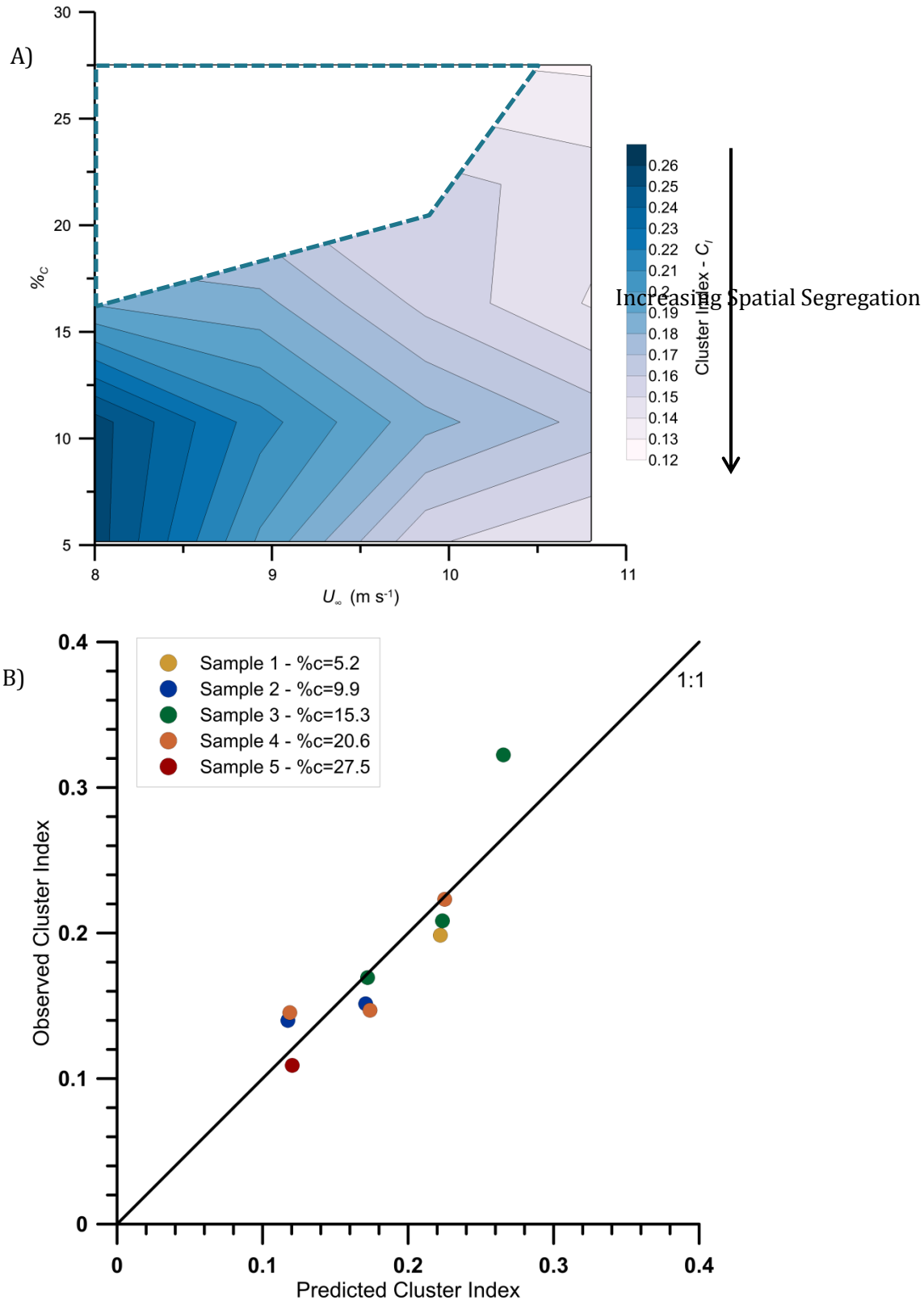

Figure 3-12 A) Response surface plot illustrating the relationship of the cluster index to U_∞ and $\%_C$. B) Multivariate statistical model of the cluster index, illustrating strong agreement between predicted values and observed values.

3.8 Ripple Genesis – The Story of an Aeolian Impact Ripple

To synthesize the previous discussion of morphometric and optical approaches to the analysis of aeolian impact ripple development in bimodal sand beds, the following is a review of a single wind tunnel run, that of Sample 1 at 9 m s^{-1} ($\%_C$ = 5.19, U_∞ = 8.9 m s^{-1}). This example provides a scenario in which ripple development dynamics are within the optimal range in terms of wind speed and proportion of coarse particles. Ripple genesis during the first 1000 seconds of fluid flow is illustrated in Figure 3-13. The test begins with a level sand bed of uniform thickness and thoroughly mixed particles (t = 0 s). The ripple cross section confirms that the bed surface is essentially planar, as the minor variations in bed thickness are sub-millimetre, which is less than the largest expected grain diameter.

Within 60 s (see ***A*** in Figure 3-13), minor topographic perturbations have developed from the first impacts of saltators, and the removal of surface particles from the bed. The net mass loss rate is high ($Q_{\text{out}} >> Q_{\text{in}}$), in fact the highest recorded during this experiment. Sediment is not only being moved downwind in the tunnel, but also being removed from the area of observation of the sand bed. The sediment transport system in this case is not supply or transport limited, as there are ample fine mode particles to entrain. There is a rapid increase in the β_C of the sand bed associated with the winnowing of fine particles. At this time the surface is still comprised of less than 15% coarse particles, although this is an increase of 200% over the starting value. Creep of the coarse mode particles, driven by the impacts of the saltation cloud, has been insufficient to result in a significant spatial segregation of the two particle modes, although minor areas of increased coarseness are beginning to appear. The cluster index, C_I, is decreasing, quantifying any minor spatial clustering of the two particle modes that is not visible in the other metrics.

By 320 s (see ***B*** in Figure 3-13), small impact ripples have formed. The ripples are still not fully developed, but have grown in both amplitude and wavelength from ***A*** (t = 60 s). The rate of net mass loss is declining due to both surface armouring and bedform drag (Bagnold, 1941). While particles are still moving, fewer particles are being removed from the bed. The β_C has risen since ***A*** (t = 60 s) to over 30%, a 600% increase from t = 0s, and is reaching the maximum value for this test. The large increase in β_C results in the increased sheltering of fine particles on the bed surface, and is increasing the aerodynamic roughness of the surface. This effect was apparent in Table 2-2, where Sample 4 has a fluid threshold that is 1.0 m s^{-1} higher than Sample 1. Creep has resulted in the accumulation of coarse mode particles, illustrating a clear pattern of spatial segregation, which corresponds to the ripple crests and troughs. Areas of the ripple crests are now comprised of over 70% coarse particles, while troughs contain less than 10% coarse particles. There is evidence of the downwind migration of the ripple forms with the ripple crests moving as coherent units. Some ripples have coalesced since ***A*** (t = 60 s), with slower ripples being overtaken by faster ripples. The cluster index has levelled off and is approaching the final average value, indicating that the spatial segregation of the two particle modes as measured by this index has reached its maximum. The basic form of the impact ripples has now been established for this wind speed and particle size distribution combination, and will continue to evolve with time.

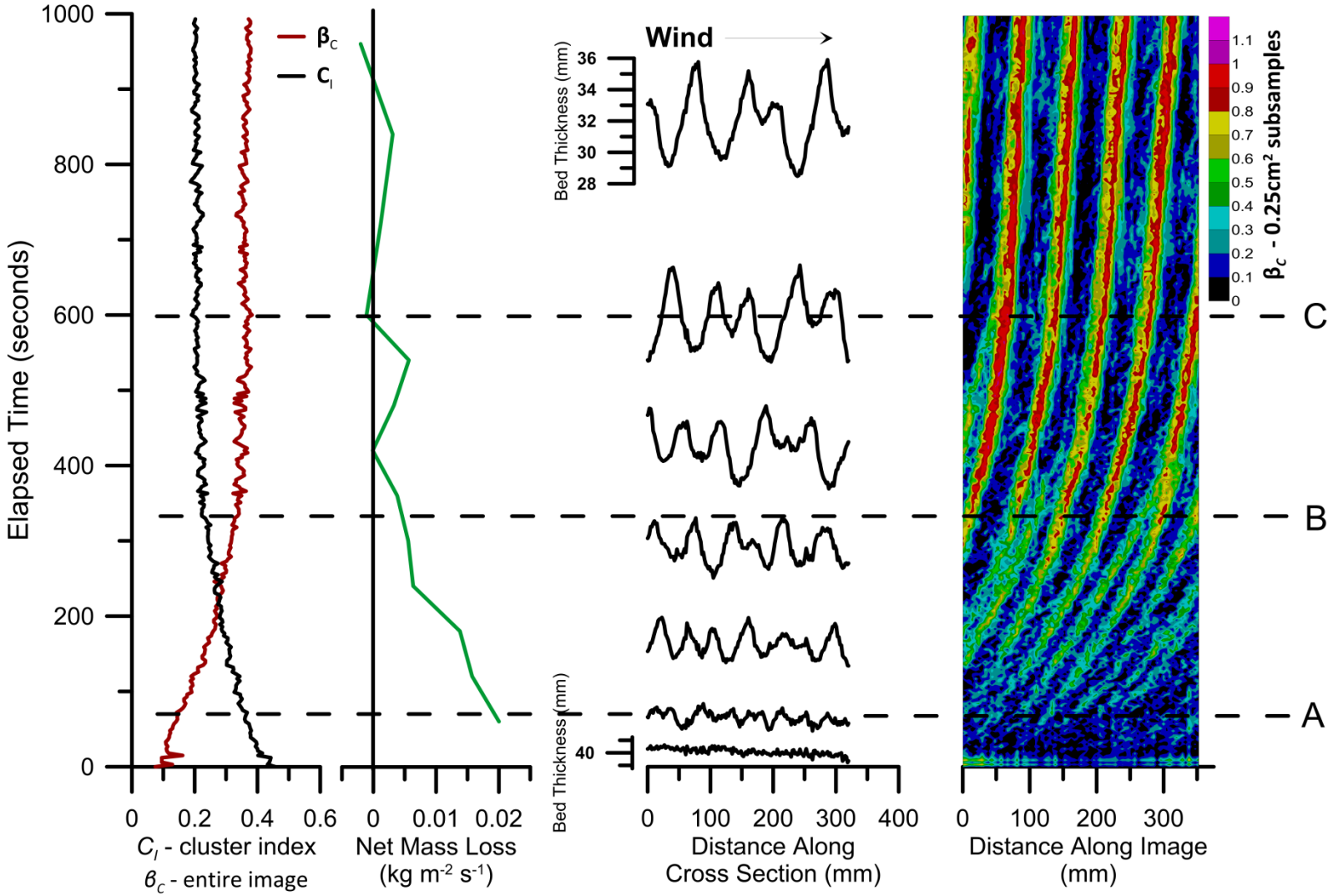

Figure 3-13 Summary plot for impact ripple genesis for Sample 1 ($\%_C$ = 5.2) at U_∞ = 9 m s^{-1}.

After ten minutes (see ***C*** in Figure 3-13), the system is approaching equilibrium. The ripples have grown in amplitude since **B** (t = 320 s). In comparison, the wavelength has changed little in numeric value, while the ripples are illustrating better defined crests and troughs. The erosion rate is approaching 0 kg m^{-2} s^{-1}, indicating that while particles may still be in motion in the system, the net removal of sediment at the measurement window has ceased ($Q_{out} \approx Q_{in}$). The surface coarseness has now stabilized, reaching β_C = 38.5%, which is nearly 800% above the initial value. The sediment transport system is limited by both the sharp decrease in the fine mode particles on the surface and the bedform drag on the fluid flow imposed by the ripples. Spatial segregation of the particle modes is very clear, with ripple crests comprised in most cases of over 80% coarse mode particles. Since **B** (t = 320 s), the coarse mode groupings have continued to migrate as coherent units in the streamwise direction. The cluster index continues to fluctuate around a mean value that will from here on remain unchanged.

After ten minutes (timeline **C**), it is clear from all displayed metrics that the system is in a state of equilibrium. Minor topographic reshaping of the ripple crests does occur, and slow migration downwind continues; however, the amplitude and wavelength characteristics do not change. The surface remains stable with $\frac{-dQ}{dt} \sim 0$ and no further change in either β_C or C_I is observed.

Chapter 4 Conclusions

For the first time in an experimental wind tunnel, aeolian impact ripples have been extensively studied in bimodal sand beds. Morphometric analysis of ripple amplitude, wavelength and ripple index revealed that both wind speed and particle size distribution governs bedform development. Optical techniques were also developed to investigate, at grain scale resolution, the influence of these factors on bedform development.

Specifically addressing the core objectives of this research (1.5, Page 18), the findings illustrate that wind speed has the greatest influence on both the ripple morphometrics and spatial organization of particle populations for aeolian impact ripples. Increasing the wind speed tends to increase both ripple amplitude and wavelength for a given sand bed. Particle size distribution characteristics influence both the ripple morphometrics and the spatial organization of particle populations by affecting the transport system dynamics. For a given wind speed, increasing the proportion of the sand bed that is made up of particles from the coarse mode will decrease both ripple amplitude and wavelength. However, this relationship is complicated when the proportions are low, as a sufficient proportion of particles must be present to produce ripples. At high wind speeds, sand beds made up of low ratios of coarse particles to fine particles are subject to high rates of net mass loss.

Particle self-organization occurs quickly, particularly within a small range of wind speed and particle size distribution combinations, and plays a key role in the formation and evolution of aeolian impact ripples. It is evident from the optical findings that once a threshold level of organization is reached, full-fledged ripples will develop.

The findings of this research could be expanded through future projects that include a broader data range, specifically by incorporating other varied ratios of particle size diameters. Performing a similar study with different ratios within the range of $3 < d_c/d_f < 7$ would expand the relationships to those shown in Equation 4-1 and 4-2. Experimental wind speeds would require adjustment to meet the criteria of particle transport mode segregation (i.e. above fluid threshold for the fine mode particles, but not above the impact threshold for the coarse mode particles)

$$\text{Amplitude} = a\,U_\infty + b\,\%_C + c\frac{d_c}{d_f} \qquad \text{Equation 4-1}$$

$$\text{Wavelength} = \text{e}\,U_\infty + \text{f}\,\%_C + \text{g}\frac{d_c}{d_f} \qquad \text{Equation 4-2}$$

Additional studies could make use of the newly developed optical analysis techniques to investigate the spatial organization of individual size fractions within a distribution at varying wind speeds. Studying a unimodal particle size distribution in this manner may reveal the varying roles that each particle size fraction plays in the development of aeolian impact ripples. Potential for optical analysis of remote sensing imagery from platforms such as the Mars Observer also exists, as image analysis and digital elevation model analysis could reveal the nature of relationships for aeolian mega ripples on extra-terrestrial planets.

Additional contributions of the research conducted for this thesis are the automation of morphometric analysis for non-contact 3D digitizers, frequently used within the Trent Environmental Wind Tunnel facility. Furthermore, this thesis required the development of original optical processing techniques for distinguishing, at the grain scale, particle size fractions. The processes developed also allow for the automated analysis of large volumes of data in a relatively short time period, helpful to future projects that choose

to take advantage of these improvements. The research and methods innovations of this thesis broaden the scope of the types of questions that can now be addressed by the scientific community, particularly within the aeolian impact ripple field.

Works Cited

Anderson, R. S., 1987. A theoretical model for aeolian impact ripples. *Sedimentology,* Volume 34, pp. 943-956.

Bagnold, R. A., 1941. *The physics of blown sand and desert dunes.* 2nd ed. London: Methuen & co.

Bettis III, A. E., 2012. Climatic and Biotic Controls on Silt Production and Accumulation of Loess. *Nature Education Knowledge,* 10(25).

Cornish, V., 1914. *Waves of sand and snow,* London: Unwin.

Dale, M. R. & Fortin, M. J., 2002. Spatial autocorrelation and statistical tests in ecology. *Ecoscience,* Volume 9, pp. 162-167.

Duran, O., Claudin, P. & Andreotti, B., 2011. On aeolian transport: Grain-scale interactions, dynamical mechanisms and scaling laws. *Aeolian Research,* 3(3), pp. 43-270.

Eastwood, E., Nield, J., Baas, A. & et al, 2011. Modelling controls on aeolian dune-field pattern evolution. *Sedimentology,* 58(6), pp. 1391-1406.

Ellwood, J. M., Evans, P. D. & Wilson, I. G., 1975. Small scale aeolian bedforms. *Journal of Sedimentary Petrology,* Volume 45, pp. 554-561.

Fortin, M. J. & Dale, M. R., 2005. *Spatial Analysis. A Guide for Ecologists.* Cambridge: Cambridge University Press.

Fryberger, S. G. & Schenk, C., 1981. Wind sedimentation tunnel experiments on the origins of aeolian strata. *Sedimentology,* Volume 28, pp. 805-821.

Gerety, K. M. & Slingerland, R., 1983. Nature of the saltating population in wind tunnel experiments with hetergeneous size-density sands.. In: M. E. Brookfield & T. S. Ahlbrandt, eds. *Eolian Sediments and Processes.* New York: Elsevier, pp. 115-131.

Golden Software Inc., 2012. *What gridding method should I use to grid my data file?.* [Online] Available at: http://www.goldensoftware.com/activekb/questions/503/ [Accessed 6 May 2012].

Gordon, M. & McKenna Neuman, C., 2011. A study of particle splash on developing ripple forms for two bed materials. *Geomorphology,* 129(1-2), pp. 79-91.

Greeley, R. & Iverson, J. D., 1985. *Wind as a geological process: on Earth, Mars, Venus, and Titan.* Cambridge: Cambridge University Press.

Greeley, R. & Peterfreund, A. R., 1981. Aeolian "megaripples": Examples from Mono craters, California and northern Iceland. *Geological Society of America Abstracts with Programs,* Volume 13, p. 463.

Isenburg, O., Yizhaq, H., Tsoar, H. & et al, 2011. Megaripple flattening due to strong winds. *Geomorphology,* 131(3-4), pp. 69-84.

Jain, A. K., 2010. Data clustering: 50 years beyond K-means. *Pattern Recognition Letters,* Volume 31, pp. 651-666.

Karnieli, A., Tsoar, H., Wenkart, R. & al., e., 2008. Morphology and dynamics of aeolian mega-ripples in Nahal Ksauy, southern Israel. *Israel Journal of Earth Sciences,* Volume 57, pp. 149-165.

Konica-Minolta, 2004. *Non-Contact 3D Digitizer Vivid 9i/VI9i-L Instruction Manual.* s.l.:s.n.

Lancaster, N., 1995. *Geomorphology of desert dunes.* London: Routledge.

Lancaster, N., Nickling, W. & Gillies, J., 2002. *Exceptionally coarse-grained wind ripples in the Wright Valley, Antarctica.* Lubbock, Texas, USA, s.n.

Lee, C.-M. & Culhane, D. P., 1998. A perimeter-based clustering index for measuring spatial segregation: a cognitive GIS approach. *Environment and Planning B: Planning and Design,* Volume 25, pp. 327-343.

Manukyan, E. & Prigozhin, L., 2009. Formation of aeolian ripples and sand sorting. *Physical Review,* 79(3).

Mathworks Inc., 2012. *imresize().* [Online]
Available at: http://www.mathworks.com/help/toolbox/images/ref/imresize.html
[Accessed 7 May 2012].

McKenna Neuman, C., 2003. Effects of temperature and humidity upon the entrainment of sedimentary particles by wind. *Boundary-Layer Meteorology,* Volume 108, p. 61–89.

McKenna Neuman, C., 2004. Effects of temperature and humidity upon the transport of sedimentary particles by wind. *Sedimentology,* Volume 51, pp. 1-17.

McKenna Neuman, C., Boulton, J. W. & Sanderson, S., 2009. Wind tunnel simulation of environmental controls on fugitive dust emissions from mine tailings. *Atmospheric Environment,* 43(3), pp. 520-529.

McKenna Neuman, C. & Maljaars, M., 1997. Wind tunnel measurement of boundary-layer response to sediment transport. *Boundary-Layer Meteorology,* Volume 84, pp. 67-83.

Milana, J., 2009. Largest wind ripples on Earth?. *Geology,* Volume 37, pp. 343-346.

Milana, J. P., Forman, S. & Krohling, D., 2010. The largest wind ripples on Earth: reply. *Geology Forum,* pp. e219-e220.

Neild, J. M. & Baas, A. C., 2008. Investigating parabolic and nebkha dune formation using a cellular automaton modellling approach. *Earth Surface Processes and Landforms,* 33(5), pp. 724-740.

O'Brien, P. & McKenna Neuman, C., 2012. A wind tunnel study of particle kinematics during crust rupture and erosion. *Geomorphology,* Volume 173-174, pp. 149-160.

Pye, K. & Tsoar, H., 1990. *Aeolian sands and sand dunes.* North Yorkshire: Cambridge University Press.

Sakamoto-Arnold, C. M., 1981. Eolian features produced by the December 1977 windstorm, southern San Joaquin Valley, California. *Journal of Geology,* Volume 89, pp. 129-137.

Seppälä, M. & Lindé, K., 1978. Wind tunnel studies of ripple formation. *Geografiska Annaler,* Volume 60, pp. 29-42.

Shaio, Y., 2008. *Physics and modelling of wind erosion.* New York: Springer.

Sharp, R., 1963. Wind Ripples. *The Journal of Geology,* Volume 71, pp. 617-636.

Shortridge, A., 2007. Practical limits of Moran's autocorrelation index for raster class maps. *Computers, Environment and Urban Systems,* 31(3), pp. 362-371.

Wang, Y., Wang, D. W., Wang, L. & Zhang, Y., 2009. Measurement of sand creep on a flat sand bed using a high-speed digital camera. *Sedimentology,* 56(6), pp. 1705-1712.

Willetts, B. B. & Rice, M. A., 1988. Particle dislodgement from a flat sand bed by wind. *Earth Surface Processes & Landforms,* Volume 13, pp. 717-728.

Yang, Y., Chen, S., et al & Gu, M., 2009. New inflow boundary conditions for modelling the neutral equilibrium atmospheric boundary layer in computational wind engineering. *Journal off Wind Engineering and Industrial Aerodynamics,* 97(2), pp. 88-95.

Yizhaq, H., 2005. A mathematical model for aeolian megaripples on Mars. *Physica A: Statistical Mechanics and its Applications,* 357(1), pp. 57-63.

Yizhaq, H., 2008. Aeolian Megaripples: Mathematical Model and Numerical Simulations. *Journal of Coastal Research,* Volume 246, pp. 1369-1378.

Yizhaq, H., Balmforth, N. J. & Provenzale, A., 2004. Blown by wind: nonlinear dynamics of aeolian sand ripples. *Physica D: Nonlinear Phenomena,* 195(3-4), pp. 207-228.

Appendix I

Moran's I Autocorrelation Statistic

The values of *I* range from -1 through 1, with values closer to 1 generally indicating positive spatial autocorrelation, and values closer to -1 indicating the opposite (Shortridge, 2007). Moran's I is calculated using Equation A-1. The value of y_i is the central pixel being compared to the average value of the pixel neighbourhood, $\bar{y}$, and the other pixels in the neighbourhood, y_j. A contiguity matrix which defines the influence of neighbouring elements is incorporated into the equation, in the form of w_{ij}. The contiguity matrix has a sum of 1, with numeric values found in Table A-1.

$$I = \frac{n}{\sum_{i}^{n}\sum_{j}^{n} w_{ij}} \bullet \frac{\sum_{i}^{n}\sum_{j}^{n} w_{ij}(y_i - \bar{y})(y_j - \bar{y})}{\sum_{i}^{n}(y_i - \bar{y})^2} \qquad \text{Equation A-1}$$

Table A-1 Contiguity Matrix for Moran's I statistic

0.1036	0.1464	0.1036
0.1464	0	0.1464
0.1036	0.1464	0.1036

In other words, Moran's I should describe the degree to which coarse particles are segregated from fine particles on the surface of the sand bed. If a coarse or fine particle, represented by pixel value of 1 or 255 respectively, is surrounded entirely by similar values, Moran's *I* for that pixel is 1. Dissimilar values within the neighbourhood result in a value of less than 1. The mean of individual values is reported for the area under analysis; in this case, an entire image.

Moran's *I* is a computationally intensive statistic to calculate, and did not return any useful results. There was no correlation to other metrics measured, especially surprising when considering the nature of β_C. Moran's I for each image in a test run is shown in Figure A-1, with β_C plotted for comparison. This finding results from the large number of pixels, over four million, making up the images. The statistic is reported as an average value for the entire image, and it is entirely possible to have large areas of the image with $I < 0$, and still report a highly positive value.

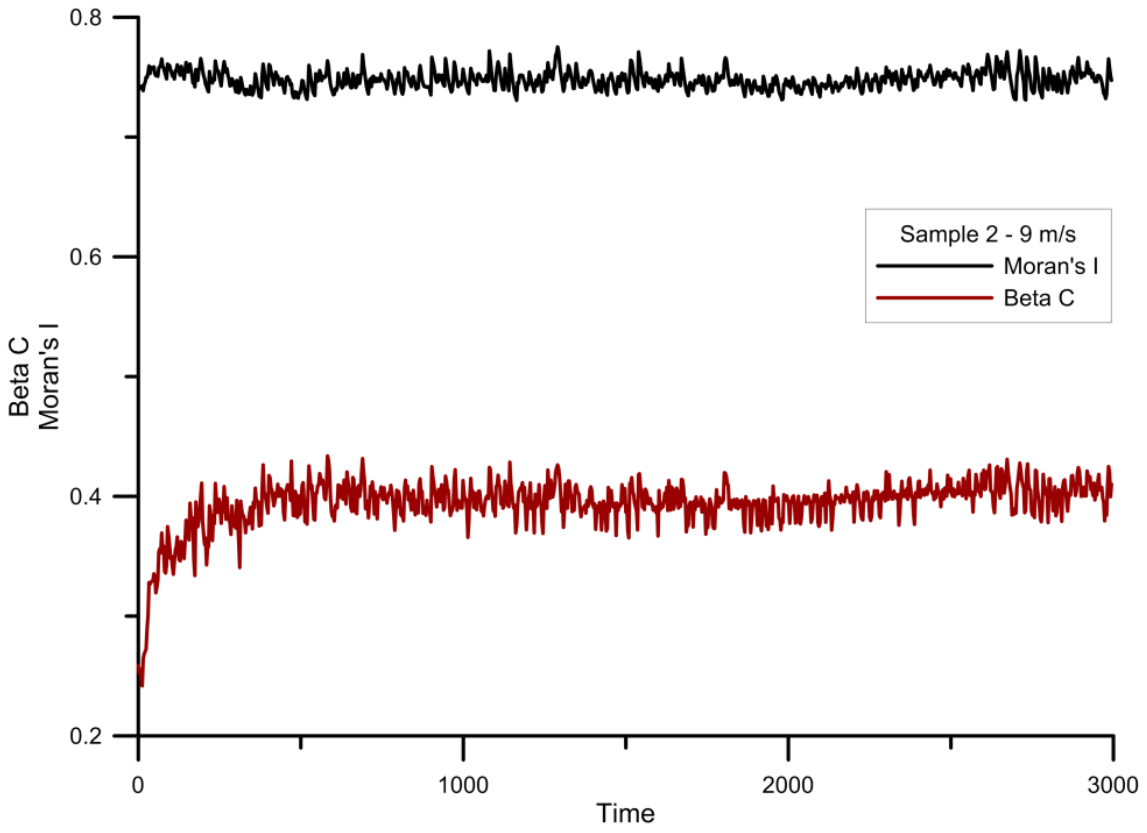

Figure A-1 Illustration of Moran's I and β_C, showing no sensitivity of *I* to a changing bedform.

Shortridge (2007) published a detailed analysis of the "Practical limits of Moran's I for raster class maps", in which matrices of known spatial autocorrelation were studied, yet the "relatively-large raster framework (250 x 250 pixel)" used was far smaller than the

1632 x 2464 pixel images analyzed in this thesis. Large areas of the images covered by coarse particles, will have the same values as areas of the image covered in fine particles. In the case of this study, Moran's I acts more as a boundary detection algorithm than a spatial statistic.

To illustrate how the calculation of Moran's I at boundaries of coarse mode and fine mode pixels is represented, Figure A-2 shows the process for an idealized image, consisting of two distinct colours. It is clear that large areas of the images are represented by $I = 1$, and only the boundary contains values of $I < 1$.

Original Image	Classified Image	Moran's I Values
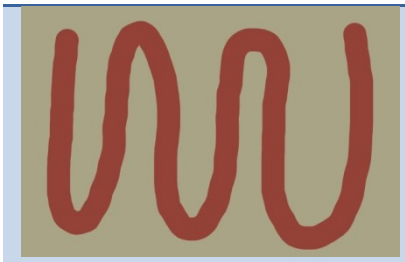	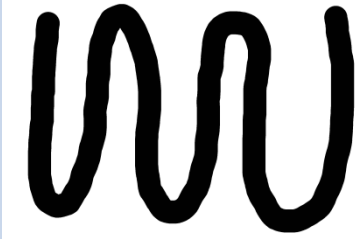	
$\beta_C = 0.3193$	$\beta_C = 0.3193$	$\bar{I} = 0.9881$ $I_{=1}$ - 98.80% $I_{min} = -0.1080$

Figure A-2 The original image is converted into the classified black and white image where fine mode particles are represented by pixel values of 255 (white) and coarse mode particles are represented by pixel values of 0 (black). Moran's I values of 1 are represented by areas of white, while grey pixels represent *I* values of less than 1. The presence of boundaries is obvious.

A proper boundary detection algorithm quantifies the boundary length between the two particle colours by providing a count of the number of pixels that are considered boundary. Moran's I is highly computationally intensive, and faster boundary detection algorithms are available to accomplish the same task.

Appendix II

The digital nature of this thesis extends into the appendix, where a number of the scripts, functions, videos and results are contained. The accompanying DVD contains the following:

Folder Name	Description
Matlab code	Contains Mathworks Matlab functions in .txt format
Results – Plots	Contains high quality (600 dpi) versions of results in .png format
Scripter scripts	Contains Golden Software Scripter scripts in .txt format
Videos	Contains animated sequences of optical data files for each of the test runs